

A Modern View of Perturbative QCD and Application to Heavy Quarkonium Systems*

Y. SUMINO

*Department of Physics, Tohoku University
Sendai, 980-8578 Japan*

Abstract

Perturbative QCD has made significant progress over the last few decades. In the first part, we present an introductory overview of perturbative QCD as seen from a modern viewpoint. We explain the relation between purely perturbative predictions and predictions based on Wilsonian effective field theories. We also review progress of modern computational technologies and discuss intersection with frontiers of mathematics. Analyses of singularities in Feynman diagrams play key roles towards developing a unified view. In the second part, we discuss application of perturbative QCD, based on the formulation given in the first part, to heavy quarkonium systems and the interquark force between static color charges. We elucidate impacts on order Λ_{QCD} physics in the quark mass and interquark force, which used to be considered inaccessible by perturbative QCD.

* Lecture given at “QCD Club,” on 12 June 2014 at Univ. of Tokyo, Japan.

Contents

1	Introduction	2
2	Quick Overview of Perturbative QCD	3
2.1	What is perturbative QCD?	3
2.2	Remarkable progress of computational technologies in the last 10-20 years	4
2.3	Comment on Impacts on Physics Insights	6
3	Overview of Perturbative QCD in More Detail	6
3.1	Perturbative expansion in α_s	6
3.2	OPE in a Wilsonian effective field theory	10
3.3	Dimensional regularization and IBP identities	12
3.4	Asymptotic expansion of diagrams and relation to EFT	14
3.5	Higher-loop integrals and multiple zeta values	18
3.6	Closing the first part: summary and benchmarks	22
4	Application to Heavy Quarkonium Systems	25
4.1	IR contributions in the static QCD potential	25
4.2	UV contributions as a “Coulomb+linear” potential	31
4.3	Implication and physical interpretation	34
4.4	Lessons drawn from the analysis of heavy quarkonium states	38
5	Concluding Remarks	38

1 Introduction

More than 40 years have passed since the birth of QCD. Accordingly there already exists plenty of accumulated knowledge in perturbative QCD owing to its history. Let us quote a note written by the late Kodaira in 2005 [1], which summarizes the history of perturbative QCD very briefly: In the first decade from the mid-1970s, correctness of perturbative QCD was confirmed qualitatively, whereas quantitative predictions were found to be difficult due to existence of very large radiative corrections; the second decade from the mid-80s was a time of contemplation, during which the research field was subdivided and specialized, and people went deeply into difficult problems; in the third decade from the mid-90s, solutions to these problems were found and perturbative QCD was progressively formulated as precision science, where predictions for observables in high-energy physics with order 10% accuracy were becoming available.

Another decade has passed since then. In the meantime, the accuracy as precision science improved further, and many new predictions appeared, which were not possible before. Broadly speaking, today one sees a high degree of sophistication achieved in every subdivided field of perturbative QCD. One finds very interesting mature researches in each of the subjects, such as, jet physics, B physics, physics of deep inelastic scattering, top quark physics, quarkonium physics, etc. In addition there are developments which are common to or interconnect different fields of perturbative QCD, mainly in computational technologies. There are excellent reviews on these subjects [2, 3, 4, 5, 6, 7].

The first part of this lecture is intended to present an overview of perturbative QCD to non-experts, including graduate course students. Given the current status of being subdivided into specialized fields, it is not easy for most people to obtain a good perspective over the whole of perturbative QCD. Nevertheless, we find that there is a flow in recent developments, which may become a useful notion for developing a unified view of perturbative QCD across various subdivided fields. In this lecture, we raise attention on this flow and try to provide a perspective from a unified viewpoint. Although this is the aim, the author excuses in advance that the contents are much influenced by his own research career and would be biased, as it is highly non-trivial to understand the details of perturbative QCD in various subjects, reconstruct them and extract the essence. It should be noted that there are many important concepts and useful frameworks which are not covered by this lecture. In particular, it is a marked deficit that this lecture barely covers developments of perturbative QCD related to the LHC physics, which are actively evolving at this moment and many of which are yet to be formulated in a well organized way.

We pay particular attention to singularities in Feynman amplitudes as a key in formulating perturbative QCD. Perturbative QCD is a theoretical tool for elucidating dynamics of QCD and giving quantitative predictions to various phenomena of QCD. Hence, our tasks in perturbative QCD are to understand the nature of its large radiative corrections and to give their quantitative descriptions. To realize the tasks, the main theoretical issues can be boiled down to the following two points: (1) To develop a method on how to decompose and systematically organize the radiative corrections, and (2) to elucidate

the nature of the radiative corrections contained in the individual parts of the decomposition (which are simplified by the decomposition). Singularities in amplitudes play key roles in both of these issues.

To realize (1), theoretical frameworks such as factorization, various effective field theories (EFTs) and operator product expansion (OPE) have been exploited. In a modern language, we can develop these frameworks utilizing singularities in Feynman amplitudes. It is different from, as well as complementary to, the conventional methods which divide integral regions in momentum space into separate domains. (In this lecture we take Wilsonian EFTs and OPE as representatives of these methods, although the factorization framework [8], which is conceptually close, deserves an extensive explanation on its own.)

To understand the nature of the radiative corrections in (2), there are on-going efforts in the areas covering both mathematics and physics. It has been known empirically that, in computations of higher-order radiative corrections, final analytical results turn out to be surprisingly compact and simple, in comparison to an enormous amount work required at intermediate stages. While singularities of Feynman amplitudes must be playing crucial roles behind this empirical fact, there are unsolved questions towards understanding the mechanism. We review basic knowledge and some recent aspects.

In the latter part of this lecture, we discuss an application of perturbative QCD to heavy quarkonium systems using the above formulation. Detailed properties of heavy quarkonium systems can be investigated both qualitatively and quantitatively thanks to recent developments of perturbative QCD. Although there exist a wide variety of studies on heavy quarkonium [9, 10], we do not present a survey of those studies. In this lecture we review the studies with respect to more fundamental properties and show that the formulation of perturbative QCD works consistently. In particular we clarify the relation between the intrinsic QCD scale ($\Lambda_{\text{QCD}} \approx 300 \text{ MeV}$) and properties of the static QCD potential at $r \lesssim \Lambda_{\text{QCD}}^{-1}$. We also provide physical interpretations.

The lecture is organized as follows. (See also the table of contents in page 1.) In Sec. 2 we give a quick overview of perturbative QCD. In Sec. 3 we present more details of the overview. These sections deal with the formulation of perturbative QCD. Its application to heavy quarkonium systems is reviewed in Sec. 4. Concluding remarks are given in Sec. 5. We give a proof of a relation concerning properties of the static potential in the Appendix.

2 Quick Overview of Perturbative QCD

2.1 What is perturbative QCD?

Today, when people refer to “perturbative QCD predictions,” one notices that they can be classified into (at least) three different types. One should be careful, since without properly distinguishing between them, one may be led to confusions and eventually to unwanted errors. These three types can be defined as follows:

- (a) Prediction of an observable in the series expansion in α_s .
- (b) Prediction of an observable in the framework of a Wilsonian EFT.
- (c) Prediction of an observable assisted by model predictions.

The prediction (a) is literally a perturbative expansion of an observable in the strong coupling constant α_s . The observable needs to be free of IR divergences. Although the prediction is purely perturbative, it is known to contain intrinsic uncertainties in powers of Λ_{QCD} in the form $\sim (\Lambda_{\text{QCD}}/E)^n$, where n is some positive integer dependent on the observable and $E(\gg \Lambda_{\text{QCD}})$ denotes a scale associated with the observable (e.g. the center-of-mass energy for a total cross section).

In the prediction (b), one performs OPE within a low energy EFT. It gives a systematic expansion of an observable in powers of Λ_{QCD}/E . In this formulation, uncertainties in (a) is replaced by non-perturbative matrix elements. One should not, for instance, add a non-perturbative quantity of the prediction (b) to the prediction (a), which is an error one could make without recognizing it.

The prediction (c) is less solid compared to (a) and (b). While the main part of the prediction (c) is given by a literal perturbative expansion of type (a), the prediction also includes parts which are not based on QCD. Theoretical predictions of various observables in high-energy experiments (in particular hadron collider experiments) depend on hadronization models and parton distribution functions (PDFs). These are necessary ingredients in Monte Carlo (MC) simulations used to compare theoretical predictions with experimental data. While final states in perturbative QCD include quarks and gluons, in real experiments we observe instead hadrons in final states, hence quarks and gluons need to be hadronized in relating theoretical predictions to experimental data. Predictions of hadronization processes rely on models such as string hadronization models and cluster hadronization models. These models are, however, difficult to relate to QCD at the fundamental level. On the other hand, the distributions of quarks and gluons inside the initial proton and/or antiproton are described by PDFs. To predict PDFs we need an initial condition for the evolution equation. At present it is difficult to predict the initial condition from the first principle of QCD and they are replaced by some ansatz or a prediction by a model. Systematic uncertainties originating from these model predictions are difficult to control with high precision. Typically order 10% accuracy is achieved for this type of predictions of observables in LHC experiments, although details depend very much on observables.*

2.2 Remarkable progress of computational technologies in the last 10-20 years

Development of perturbative QCD in the last ten to twenty years has been largely based on remarkable progress of computational technologies during this period. In this short

* The difference of type (b) and type (c) predictions is that the former is systematic while the latter is not in parameterizing the part which are difficult to compute from the first principles of QCD.

overview we would like to emphasize especially developments in the following fields of technologies:

- (i) Higher-loop corrections[†]
- (ii) Lower-order (NLO/NLL) corrections to complicated processes
- (iii) Factorization of scales in loop corrections

Computations of higher-loop corrections [(i)] can essentially be regarded as processes of resolution of singularities in multi-loop integrals. Both numerical and analytical methods have been developed to evaluate higher-loop corrections. Concerning numerical methods, an essential problem has been solved by application of the theorem on resolution of singularities [11]. There exist certain algorithms (known as sector decomposition [12, 13]) to resolve any type of singularities in numerical loop computations by a finite number of steps. Thus, we can achieve higher-loop computations as we increase computational power that can be invested. (There have also been many studies on improving efficiencies of algorithms for numerical evaluations.) On the other hand, general algorithms have not been found yet for analytic evaluation of higher-loop corrections. There have been many developments in this direction, and we see rich activities in the fields which overlap with frontiers of mathematics.

Strongly motivated by the LHC experiments, rapid progress is taking place in a variety of technologies to compute lower-order [next-to-leading order (NLO) or next-to-leading logarithmic (NLL)] corrections to complicated processes [(ii)]. These technologies enable us to cope with proliferation of Feynman diagrams and existence of many kinematical variables. These technologies provide practical computational tools, often in conjunction with MC event generators. Nevertheless, at present these exploited technologies still consist of a collection of various separate techniques and a general or systematic theoretical formulation is not yet available.

Factorization of energy scales in a Feynman diagram can be realized by a method called asymptotic expansion or integration by regions of a loop integral [(iii)] [14]. This technology provides a precise foundation for constructing Wilsonian EFTs. It enables us to compute efficiently higher-order corrections to Wilson coefficients in EFTs. As a variety of EFTs have been formulated to tackle different physics targets using perturbative QCD, this technology has become an indispensable tool for computations.

A salient feature of all the above technologies is that they rely on dimensional regularization as the common theoretical basis. Perhaps the name “dimensional regularization” does not describe its characteristics appropriately; it is essentially a regularization by analytic continuation of loop integrals. This regularization method is contrasting to,

[†] Some examples of the higher-loop computations we are concerned here are the 4-loop coefficient of the beta function, 4-loop coefficient of the anomalous dimension, 4-loop correction to the R -ratio, 3-loop correction to the pole- $\overline{\text{MS}}$ mass relation, 3-loop correction to the static QCD potential, etc. We should also include many higher-loop computations related to LHC physics, such as the Higgs production cross section at next-to-next-to-leading order (NNLO), where the boundary between the technologies (i) and (ii) becomes somewhat obscure.

as well as complementary to, more conventional cut-off regularization methods which were primarily used in the early days of loop computations. In particular, dimensional regularization permits use of analyticity of loop integrals flexibly.

2.3 Comment on Impacts on Physics Insights

Let us briefly comment on impacts of the above developments of perturbative QCD on physics insights, namely new interpretations, viewpoints or concepts in physics which resulted from the developments. We find that, to date, these impacts are scattered over various specific fields within perturbative QCD. Indeed, the developments of perturbative QCD revealed rich structures in these specialized subjects individually. On the other hand, we fail to extract general concepts covering all or most of them, and we are yet to frame a general overview.

One may find some examples in the following subjects. Construction of various EFTs and accurate predictions based on them triggered new paradigms, such as heavy quark effective theory (HQET) for b -physics, or soft-collinear effective theory (SCET) for jet physics. Another example is an impact on $\mathcal{O}(\Lambda_{\text{QCD}})$ physics in the heavy quark mass and interquark force. Apparently there exists a belief that powers of $\Lambda_{\text{QCD}} = \mu \exp[-2\pi/(\beta_0\alpha_s)]$ cannot appear in perturbative expansions *at all*, since the expansion of Λ_{QCD} in α_s vanishes to all orders. Recent studies show, however, that this is not necessarily the case. We will explain the latter example in Sec. 4.

3 Overview of Perturbative QCD in More Detail

In this section we explain further details of the aspects of perturbative QCD explained in Secs. 2.1 and 2.2. Nonetheless, we do *not* cover the subjects in (c) of Sec. 2.1 and (ii) of Sec. 2.2, since we consider that we have not yet reached to a stage to discuss theoretical formulation of these subjects concisely.

3.1 Perturbative expansion in α_s

Perturbative QCD is a theory of quarks and gluons based on the QCD Lagrangian $\mathcal{L}_{\text{QCD}}(\alpha_s, m_u, m_d, m_s, \dots; \mu)$, where m_q denotes the mass of the quark q and μ denotes the renormalization scale. A perturbative prediction of an observable is given as a series expansion in α_s , whose expansion coefficients are given as functions of m_q , μ and kinematical variables. The perturbative prediction has the same input parameters as the full QCD. Usually the renormalization scale μ is not considered as an input parameter but rather a parameter used to estimate stability and uncertainties of the prediction. The prediction is systematic in the sense that it has its own way of estimating errors (without comparing to the corresponding experimental value), by using the μ dependence as well as by examining convergence of the series expansion. In this regard, perturbative QCD differs from models, which generally do not have systematic ways to estimate errors and have more input parameters than the full QCD. Fig. 1 shows schematically typical μ

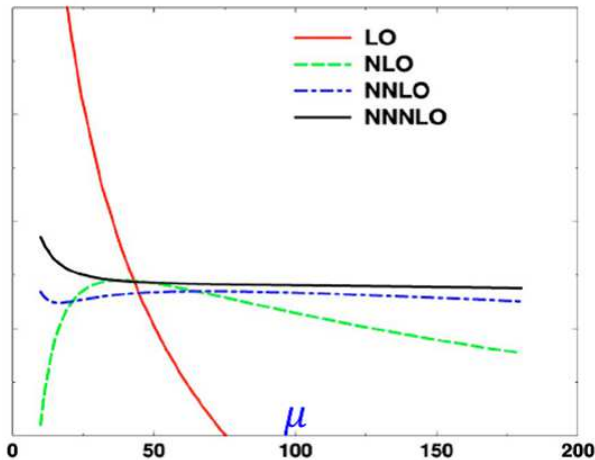


Figure 1: Plot showing schematically renormalization scale (μ) dependence of a prediction of a physical observable in perturbative QCD.

dependence of a perturbative prediction as we increase the order of the expansion. Since the all-order prediction is formally independent of μ , we observe that the μ dependence decreases as we include higher-order terms.

There are two classes of observables which are considered to be predictable by perturbative expansions in α_s . The first class consists of inclusive observables with respect to final-state hadrons. The most well-known example is the R -ratio:

$$R(E) \equiv \frac{\sigma(e^+e^- \rightarrow \text{hadrons}; E)}{\sigma(e^+e^- \rightarrow \mu^+\mu^-; E)} = \sum_q 3Q_q^2 \left[1 + \sum_{n=1}^{\infty} c_n(E/\mu) \alpha_s^n \right]. \quad (1)$$

Other observables in this class include decay widths of a non-colored particle (such as the tau lepton, weak boson, Higgs boson, etc.) or distributions of non-colored particles (such as lepton energy distribution) after integrating over the phase space of final-state hadrons. In perturbative QCD we compute these observables with respect to final-state partons (quarks and gluons) instead of hadrons, integrating over their phase space. We compare these observables with the experimental values assuming that effects of hadronization can be neglected. Logically this corresponds to assuming that the complete Fock space spanned by hadron states is equivalent to the space spanned by the states of free partons.* The identification of inclusive observables for hadronic and partonic final states is a testable hypothesis, by comparing predictions to experimental data. So far this hypothesis seems to work reasonably well.

The second class of observables are those of heavy quarkonium states. The heavy quarkonium states are the only known hadronic states, whose individual properties can be predicted using perturbative QCD, due to the heavy mass of quarks and asymptotic

* This is a highly non-trivial assumption under the existence of color confinement and spontaneous chiral-symmetry breakdown in QCD.

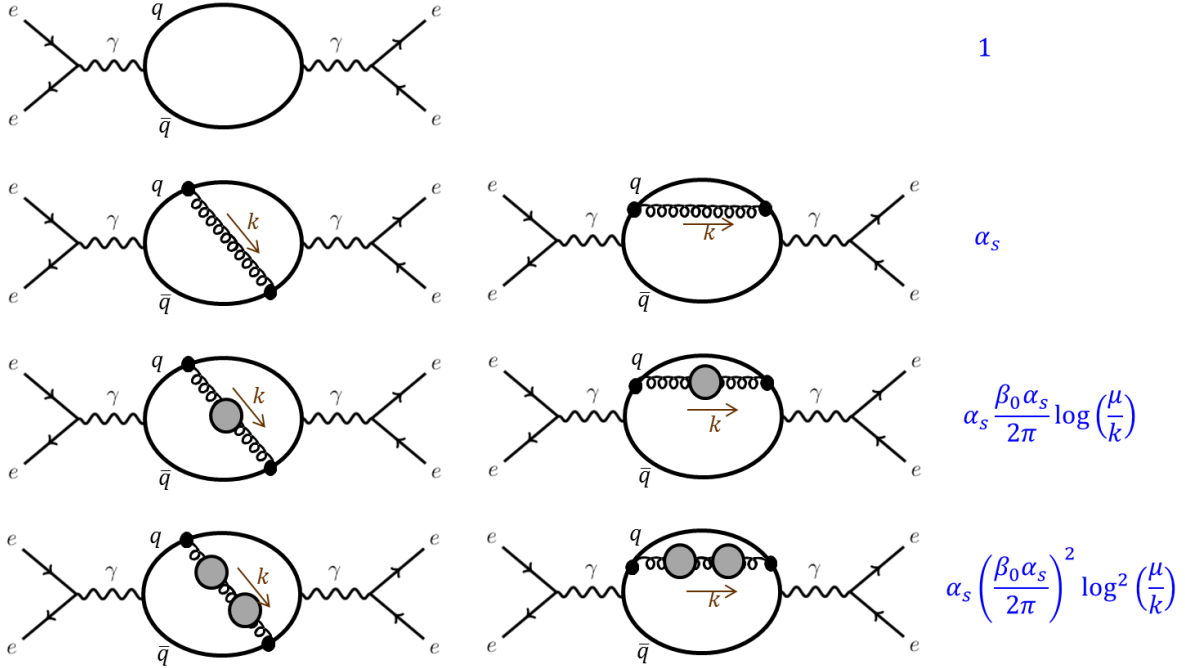


Figure 2: Class of diagrams called bubble-chain diagrams contributing to the forward scattering amplitude for $e^+e^- \rightarrow e^+e^-$. The bubble in the diagrams represents the sum of the one-loop self-energy diagrams of the gluon.

freedom of QCD. Specifically we can compute their energy spectrum, decay width, leptonic branching ratios,[†] and transition rates. We will discuss the energy levels of heavy quarkonium states in Sec. 4.

As already mentioned, a prediction given as a perturbative series in α_s generally contains uncertainties of order $(\Lambda_{\text{QCD}}/E)^n$. These uncertainties originate from IR sensitivities of higher-order corrections and are referred to as contributions of “IR renormalons” [15]. We explain how the uncertainties arise, taking the R -ratio as an example.[‡]

According to the optical theorem, the R -ratio can be computed from the imaginary part of the forward scattering amplitude for $e^+e^- \rightarrow e^+e^-$. In Fig. 2, we show a class of Feynman diagrams, known as bubble-chain diagrams, relevant for this computation. (The bubble in the diagrams represents the sum of the one-loop self-energy diagrams of the gluon.) The displayed diagrams at $\mathcal{O}(\alpha_s^0)$ and $\mathcal{O}(\alpha_s^1)$ are the only ones that contribute at these orders. At $\mathcal{O}(\alpha_s^2)$ and beyond, the diagrams shown in the figure are only part of the whole contributions. As indicated in the figure, before integrating

[†] These can be translated to production cross sections in e^+e^- collisions.

[‡] The explanation given below is slightly sloppy and is correct only qualitatively. In a more solid argument, one should carefully choose a gauge-independent formulation (such as to choose the background gauge or to use the “large- β_0 approximation” [16]). Quantitatively it also matters how to fix the non-logarithmic term of the one-loop gluon self-energy.

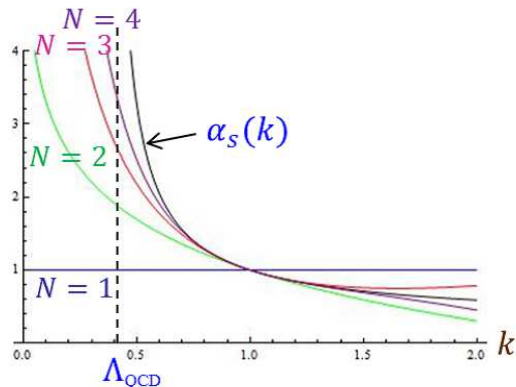


Figure 3: Plot showing k dependences of the one-loop running coupling constant $\alpha_s(k)$ [Eq. (2)] and the sums of the leading logarithms $\sum_{n=1}^N \alpha_s(\mu) [\beta_0 \alpha_s(\mu) \log(\mu/k)/(2\pi)]^{n-1}$ for $N = 1, 2, 3$ and 4. Λ_{QCD} represents the position of the pole of $\alpha_s(k)$.

over the gluon momentum k , the contribution of the bubble chain at $\mathcal{O}(\alpha_s^n)$ is given by $\alpha_s(\mu) [\beta_0 \alpha_s(\mu) \log(\mu/k)/(2\pi)]^{n-1}$. (β_0 denotes the coefficient of the one-loop beta function.) Therefore, we can incorporate the effect of the resummation of the bubble-chain diagrams to all orders by replacing the coupling constant $\alpha_s(\mu)$ in the $\mathcal{O}(\alpha_s)$ diagrams by the one-loop running coupling constant

$$\alpha_s(k) = \frac{\alpha_s(\mu)}{1 - \beta_0 \alpha_s(\mu) \log(\mu/k)/(2\pi)} = \frac{2\pi}{\beta_0 \log(k/\Lambda_{\text{QCD}})}. \quad (2)$$

The following characteristic feature of the running coupling constant is relevant: it becomes large at IR and this occurs at the intrinsic QCD scale Λ_{QCD} . In a similar manner, the effect of the bubble-chain diagrams at each order can be incorporated by replacing the coupling constant $\alpha_s(\mu)$ in the $\mathcal{O}(\alpha_s)$ diagrams by the factor $\alpha_s(\mu) [\beta_0 \alpha_s(\mu) \log(\mu/k)/(2\pi)]^{n-1}$. Fig. 3 shows the summation of this factor up to $\mathcal{O}(\alpha_s^N)$ for $N = 1, 2, 3$ and 4. One can see that as the higher-order diagrams are incorporated the sum of the bubble-chain contributions approaches the running coupling constant $\alpha_s(k)$. This shows that, although at each order the scale Λ_{QCD} does not appear explicitly, the higher-order corrections know about this intrinsic scale and know that the strong interaction becomes strong at this scale.

The consequences of incorporating these higher-order diagrams are as follows. If we estimate the perturbative series in eq. (1) by these bubble-chain contributions, the series diverges at high orders, reflecting the increase of the higher-order contributions in the IR region.[§] Therefore, the series is (at best) asymptotic and there is a limitation in

[§] The important point is that $\alpha_s(k)$ becomes large at $k \sim \Lambda_{\text{QCD}}$ rather than it has a pole at this scale. For instance, the series is similarly divergent in the case that we incorporate the effects of the two-loop coefficient of the beta function when its sign is taken to be opposite to that of the one-loop coefficient. In this case the running coupling has an IR fixed-point and therefore is finite down to $k = 0$.

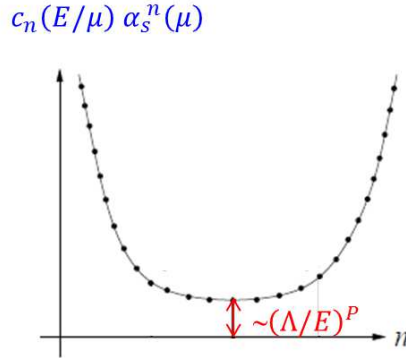


Figure 4: Diagram showing typical n -dependence of a perturbative series of an observable, based on renormalon estimates. In the case of the R -ratio, $P = 4$.

the achievable accuracy of the prediction even if we know the perturbative series up to arbitrarily high orders. Namely, until the order $n_0 \approx 2\pi/(\beta_0\alpha_s)$, each term c_n of the series in eq. (1) becomes smaller; it takes a minimal value $c_n \sim (\Lambda_{\text{QCD}}/E)^P$ at $n = n_0$; for $n > n_0$, c_n diverges rapidly. See Fig. 4. The appearance of the positive power of Λ_{QCD} reflects the fact that the higher-order terms know this intrinsic scale.[¶] In view of general properties of asymptotic series, we may expect that the sum of the series approaches the true value for $n < n_0$, and that the series has at least an error of order $(\Lambda_{\text{QCD}}/E)^P$.^{||} It turns out that often such estimates based on bubble-chain diagrams are good estimates of the true corrections, when the first several terms of the series are known exactly.

3.2 OPE in a Wilsonian effective field theory

Consider a Wilsonian low-energy EFT, written in terms of light quarks and gluons. Formally it can be constructed from the full QCD by integrating out high-energy modes above a factorization scale $\mu_f (\gg \Lambda_{\text{QCD}})$ in a path-integral formulation of the theory.

[¶] Generally P is a positive integer, and in the case of the R -ratio, $P = 4$.

^{||} A famous example is an asymptotic series

$$n! = \sqrt{2\pi n} n^n e^{-n} \left(1 + \frac{1}{12n} + \frac{1}{288n^2} - \frac{139}{51840n^3} - \frac{571}{2488320n^4} + \dots \right), \quad (3)$$

whose leading term is known as Stirling's formula. The difference of a truncated series and the true value is of the order of the last term of the truncated series. Hence, we can improve accuracy by including higher-order terms until we reach the minimum term of the series.

The Lagrangian of the EFT can be written in a form

$$\mathcal{L}_{\text{EFT}}(\mu_f) = \sum_i g_i(\mu_f) \mathcal{O}_i(\psi_q, \bar{\psi}_q, G_\mu), \quad (4)$$

which is a sum of operators \mathcal{O}_i composed of light quarks and gluons, whose energies and momenta are restricted to be below μ_f . The effective coupling constant $g_i(\mu_f)$ multiplying each operator is called a Wilson coefficient, which is determined such that the physics at $E < \mu_f$ is unchanged from the full QCD. This is expected to be possible by introducing infinitely many operators \mathcal{O}_i in the Lagrangian. Since $g_i(\mu_f)$'s include only effects of UV degrees of freedom ($E > \mu_f$), they can be computed reliably using perturbative QCD. In practice there are two ways to determine the Wilson coefficients. One way is to compute various S matrix elements with external momenta of order E , where $\mu_f \gtrsim E \gg \Lambda_{\text{QCD}}$, in both EFT and full QCD in expansions in α_s , and to require that both computations give the same results. This is known as a matching procedure. The other method is to apply asymptotic expansion of diagrams [14], which determines the operators and Wilson coefficients of EFT in an efficient way; we will explain this latter method in Sec. 3.4. The Wilson coefficients computed using perturbative QCD should be free of uncertainties by IR renormalons, since the region of integration (above μ_f) does not include the domain where the strong coupling constant is large. Thus, the EFT Lagrangian eq. (4) consists of Wilson coefficients, which effectively contain information on UV degrees of freedom, and operators composed of dynamical variables representing IR degrees of freedom.

We can perform an operator-product-expansion (OPE) in the EFT, for an observable $A(P)$ which includes a high scale $P(\gg \mu_f)$. An example of P is a mass of a heavy particle, whose effects enter $A(P)$ only through Wilson coefficients, since the heavy particle has been integrated out and is absent as a dynamical field of EFT. Within the EFT, we can compute the observable expressed in terms of Wilson coefficients and matrix elements of operators. Furthermore, we can perform a multipole expansion of operators, which is an expansion in terms of derivatives acting on the fields of the EFT:

$$\begin{aligned} A(P) &= g_1(\mu/P) \langle n | \mathcal{O}(x) | n \rangle + \frac{g_2(\mu/P)}{P^2} \langle n | \partial_\alpha \mathcal{O}(x) \partial^\alpha \mathcal{O}(x) | n \rangle \\ &+ \frac{g_3(\mu/P)}{P^4} \langle n | \partial_\alpha \partial_\beta \mathcal{O}(x) \partial^\alpha \partial^\beta \mathcal{O}(x) | n \rangle + \dots \end{aligned} \quad (5)$$

Here, $\mathcal{O}(x)$ represents symbolically local operators without derivatives. Each derivative operator ∂ corresponds to the energy-momentum ($\sim k$) of the fields in $\mathcal{O}(x)$. Hence, this expansion constitutes an expansion in $k/P(\ll 1)$, where k is restricted to be below $\mu_f(\ll P)$. Intuitively, short-distance physics at scale P generates fluctuations of color charges.

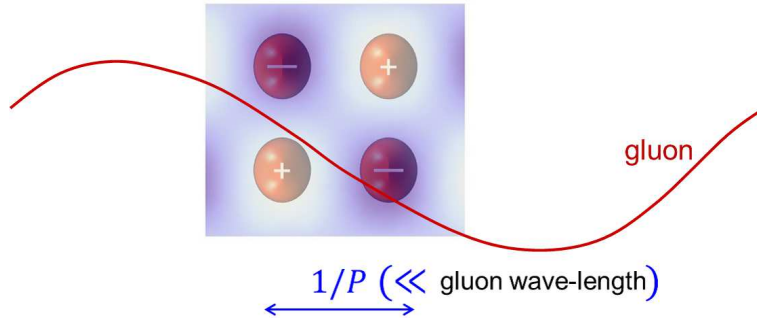


Figure 5: Intuitive picture of multipole expansion in an EFT. Gluons in the EFT have wave-lengths much larger than the typical scale $1/P$ of color-charge fluctuations. Hence, it is natural to express gluon fields by multipole expansion.

They are naturally regarded as superpositions of color multipoles from the viewpoint of light quarks and gluons whose wave-lengths are much larger than the fluctuation scale. See Fig. 5. This is in analogy to classical electrodynamics, in which an electric field at a large scale (compared to the scale of charge distribution) can be expressed generally as a superposition of electric fields generated by electric multipoles.

In eq. (5) contributions from IR degrees of freedom are contained in matrix elements of operators. They cannot be evaluated by perturbative QCD since dominant contributions come from the scale of order Λ_{QCD} . Rather these matrix elements are treated as non-perturbative quantities (parameters), which appear commonly in predictions of many observables. Well-known examples are the local gluon condensate and chiral quark condensates, which are the lowest-dimension gauge-invariant local operators of gluons and quarks, respectively. These non-perturbative matrix elements are computed by lattice simulations or determined phenomenologically from various experimental data. Hence, IR renormalons in a purely perturbative prediction of Sec. 3.1 are replaced by (or absorbed into) the non-perturbative matrix elements in the formulation of this section. As a trade-off, the Wilson coefficients can be predicted accurately (without IR renormalon uncertainties) in this formulation.

3.3 Dimensional regularization and IBP identities

Recent developments of perturbative QCD rely heavily on developments of various computational technologies. We explain some features of dimensional regularization, on which various modern technologies are based.

Let us discuss advantages and disadvantages of the dimensional regularization. Advantages can be stated as follows. (1) This regularization preserves important symmetries such as Lorentz symmetry and gauge symmetries. (2) In a single step, we can render all loop integrals and phase-space integrals finite, both at UV and IR. This is in contrast to Pauli-Villars regularization, in which one has to perform multiple subtractions according to the degree of UV divergence of an original integral. (3) There are many useful computational techniques which are possible only with this regularization [7]; we

will see some examples below.

Disadvantages can be listed as follows. (1) This regularization scheme is not well defined in the framework of quantum field theory. Since we consider the space-time dimension D as a general complex variable, (at least naively) it is not possible to consider a quantum field theory in such a dimension. This is in contrast to e.g. lattice regularization, with which a quantum field theory can be defined unambiguously. (Nevertheless, it may be worth notifying that in perturbative computations the dimensional regularization is well-defined and uniquely defined.) (2) One faces many difficulties in physical interpretations. There are typical questions beginners ask: (a) Does $1/\epsilon^n$ represent IR or UV divergences? Clearly poles in $\epsilon = (4 - D)/2$ are not equivalent to divergences, since one can write down integrals which are UV or IR divergent at $D = 4$ but free from poles in ϵ . Then, is it legitimate to identify poles in ϵ as UV divergences in the usual procedure of renormalization? (b) What is the meaning of seemingly unphysical equalities such as vanishing of a tadpole diagram $\int d^D k \frac{1}{k^2} = 0$? It is a UV divergent integral at $D = 4$, but is there a rationale or logical requirement that it must be zero?

It is certainly helpful to be aware of these advantages and disadvantages in trying to find more precise interpretations of various predictions of perturbative QCD, although it may not be necessary in carrying out practical computations.*

Probably the most powerful application of dimensional regularization is the integration-by-parts (IBP) identities [17], which we explain in the rest of this subsection. The identities are derived from the Gauss theorem in D dimension:

$$\int d^D p_1 \cdots d^D p_L \frac{\partial}{\partial X_\mu} \left(\frac{Y_\mu}{D_1^{n_1} \cdots D_N^{n_N}} \right) = 0, \quad (6)$$

$$X \in \{p_1, \cdots, p_L\}, \quad Y \in \{p_1, \cdots, p_L, q_1, \cdots, q_M\}. \quad (7)$$

Here, p_i and q_i denote a loop momentum and an external momentum, respectively; D_i denotes the denominator of an arbitrary propagator dependent on the internal and external momenta; each power n_i is an integer; in the case n_i is negative, $1/D_i^{n_i}$ represents a factor in the numerator of the integrand. The above equality is trivial in the case that the dimension D is a positive integer and if the integral is finite, since the surface term should vanish sufficiently quickly at infinity. Conceptually it is an analytic continuation of the equality to a complex dimension D (although one needs to do this carefully to be rigorous). By operating the derivative before integration, one obtains an identity among different types of loop integrals (see the example below). By choosing various X , Y and n_i 's, one can generate innumerable identities. It is a standard technology of today's loop computations to use these identities to reduce a large number of loop integrals to a small set of simple integrals (master integrals). For instance, it is not rare that order 10^3 – 10^4 loop integrals are reduced to order 10^1 – 10^2 master integrals by this reduction in contemporary loop computations.

* It took years for the author to find interpretations to the kinds of questions raised here. Now he believes (with certain reasonings) that the dimensional regularization leads to correct predictions (which should not be dependent on the regularization you choose). The reasoning helped in accomplishing tough computations.

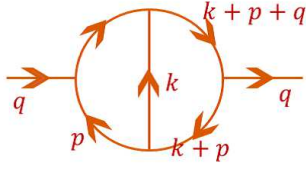


Figure 6: Two-loop Feynman diagram of massless scalar particles, which can be simplified using an IBP identity. q denotes the external momentum, while k and p denote the loop momenta.



Figure 7: Diagrams representing the IBP identity Eq. (8). The point on a line shows a two-point vertex, hence a line with a point represents the square of the corresponding propagator.

Let us take a diagram shown in Fig. 6 as an example and explain the IBP identity. All the internal lines are assumed to be massless. One can generate a following identity:

$$\begin{aligned}
0 &= \int d^D p d^D k \frac{\partial}{\partial k^\mu} \frac{k^\mu}{p^2 k^2 (k+p)^2 (p+q)^2 (k+p+q)^2} \\
&= \int d^D p d^D k \frac{1}{p^2 k^2 (k+p)^2 (p+q)^2 (k+p+q)^2} \\
&\quad \times \left[D - \frac{2k \cdot k}{k^2} - \frac{2k \cdot (k+p)}{(k+p)^2} - \frac{2k \cdot (k+p+q)}{(k+p+q)^2} \right] \\
&= \int d^D p d^D k \frac{1}{p^2 k^2 (k+p)^2 (p+q)^2 (k+p+q)^2} \left[D - 4 + \frac{p^2 - k^2}{(k+p)^2} + \frac{(p+q)^2 - k^2}{(k+p+q)^2} \right].
\end{aligned} \tag{8}$$

We suppressed $+i0$ in the propagator denominators. In the last equality we expressed the numerators in linear combinations of the propagator denominators. The last line can be regarded as a relation among the diagrams shown in Fig. 7. Since some of the diagrams are the same, in fact the identity relates three different diagrams. Note that in the last line of eq. (8) some of the propagator denominators are canceled by the numerators. As a result, the second and third diagrams of Fig. 7 have simpler topologies than the first diagram. Thus, the identity can be used to express the first diagram in terms of two diagrams with simpler topologies.

3.4 Asymptotic expansion of diagrams and relation to EFT

In this subsection we explain the technique called asymptotic expansion of a diagram or integration by regions [14]. This can be used to identify operators \mathcal{O}_i (effective interactions) in the Lagrangian of a Wilsonian EFT, eq. (4). At the same time the technique provides an efficient method for perturbative computations of Wilson coefficients $g_i(\mu_f)$.

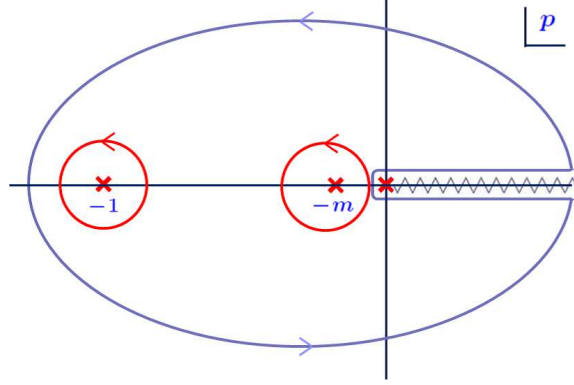


Figure 8: Analyticity of the integrand of eq. (9) in the complex p -plane. The blue contour can be deformed to the sum of the red contours.

Let us first explain the idea of the asymptotic expansion in a simplified example. We consider an integral

$$I(m; \epsilon) = \int_0^\infty dp \frac{p^\epsilon}{(p+m)(p+1)}. \quad (9)$$

It is a toy model imitating an integral in dimensional regularization. In fact, it is a one-parameter integral, imitating integral over the radial direction of a dimensionally-regulated integral, with $p^\epsilon dp$ representing a volume element; furthermore each propagator denominator is a linear function of p rather than a quadratic function. Suppose $m \ll 1$ is a small parameter and consider expanding I in m . Let us presume as if the integral region is divided into two regions $p < 1$ and $p > 1$, and expand the integrand in each region in a small parameter. Nevertheless, we restore the original integral region in each integral, as follows.

$$I = \int_0^\infty dp \underbrace{\frac{p^\epsilon}{p+m} (1 - p + p^2 + \dots)}_{p < 1} + \int_0^\infty dp \underbrace{\frac{p^\epsilon}{p+1} \frac{1}{p} \left(1 - \frac{m}{p} + \dots\right)}_{p > 1 \gg m}. \quad (10)$$

At a first glance, this seems to give a wrong result, since firstly we have extended each integral region to a region where the expansion is not justified, and secondly there would be a problem of double counting of region. Surprisingly, however, if we evaluate the individual terms of the above integrals and take their sum, it gives the correct expansion in m of the original integral I .

The reason can be understood as follows. Fig. 8 shows the analyticity of the integrand of eq. (9) in the complex p -plane: there are poles at $p = -1$ and $p = -m$; the origin is a branch point due to p^ϵ and the branch cut lies along the positive p -axis. The integral of p along the positive p -axis is equal to, up to a proportionality factor, an integral along the contour wrapping the branch cut. We may close the contour at negative infinity and deform the contour into the sum of two closed contours surrounding the two poles. (See Fig. 8: we deform the blue contour to the sum of the red contours.) Along the

contour surrounding the pole at $-m$, it is justified to expand the integrand using the fact $|p| \approx m \ll 1$; this gives the integrand of the first term of eq. (10). After the expansion, the contour of the integral of each term of the expansion can be brought back to the original contour wrapping the branch cut along the positive p -axis. Similarly, along the contour surrounding the pole at -1 , we may expand the integrand using $|p| \approx 1 \gg m$, which gives the second term of eq. (10). Again, after the expansion, the integral contour can be brought back to the one surrounding the branch cut.* In this way, we obtain eq. (10).

Thus, for an integral that imitates a dimensionally-regulated one, we can expand the integral in a small parameter, without introducing a cut-off in the integral region. The important point in the above example is that the contribution from each of the scales $|p| \sim 1$ and $|p| \sim m$ is expressed by a contour integral surrounding the corresponding pole in the integrand (i.e., by the residue of each pole).

The method for the asymptotic expansion of a loop integral in dimensional regularization is the same: we divide the integral region into separate regions according to the scales contained in the integrand and expand the integrand in appropriate small parameters in respective regions; we nevertheless integrate individual terms of the expansions over the original integral region, namely, over the entire D -dimensional phase space for each loop integral.†

For illustration we consider the following two-loop integral in the case $p^2 \ll M^2$:

$$J(p^2, M^2) = \int d^D k d^D q \frac{1}{k^2(p-k)^2[(k-q)^2 + M^2]q^2(p-q)^2}. \quad (11)$$

The corresponding diagram is shown in Fig. 9, where the thick blue line represents a heavy particle with mass M and all other lines represent massless particles. We expand J in p^2/M^2 . The integral region of each loop integral is divided into two regions: high momentum region (H), $|k| > M$ or $|q| > M$, and low momentum region (L), $|k| < M$ or $|q| < M$. Hence, the whole integral region is divided into four regions: (H,H),(H,L),(L,H),(L,L). Of these (H,L) and (L,H) are the same due to the exchange symmetry between k and q . Fig. 10 shows how to perform the asymptotic expansion in each of these regions.

In the region (L,L) we expand the massive propagator $1/[(k-q)^2 + M^2]$ in k and q . Each term represents an effective four-point vertex, where the leading vertex is given by a constant coupling $1/M^2$. This is depicted in the left-most part of the figure. Higher-order vertices are associated with powers of the factor $(k-q)^2/M^2$, which correspond to four-point interactions given by higher derivative operators.

* In these manipulations, the value of ϵ in each term needs to be varied appropriately by analytical continuation into the domain where each integral is well defined.

† At the moment, the proof of this method using contour deformation as in the above toy model is missing, for general loop integrals in dimensional regularization. While it is likely that such an interpretation is possible generally, presently this type of proof is valid only in some selective cases. There exists a general proof based on different reasonings [18].

$$= \int d^D k d^D q \frac{1}{k^2(p-k)^2[(k-q)^2 + M^2]q^2(p-q)^2}$$

Figure 9: Two-loop diagram used to illustrate asymptotic expansion in p^2/M^2 . The thick blue line represents a propagator with mass M , while all other lines represent massless propagators.

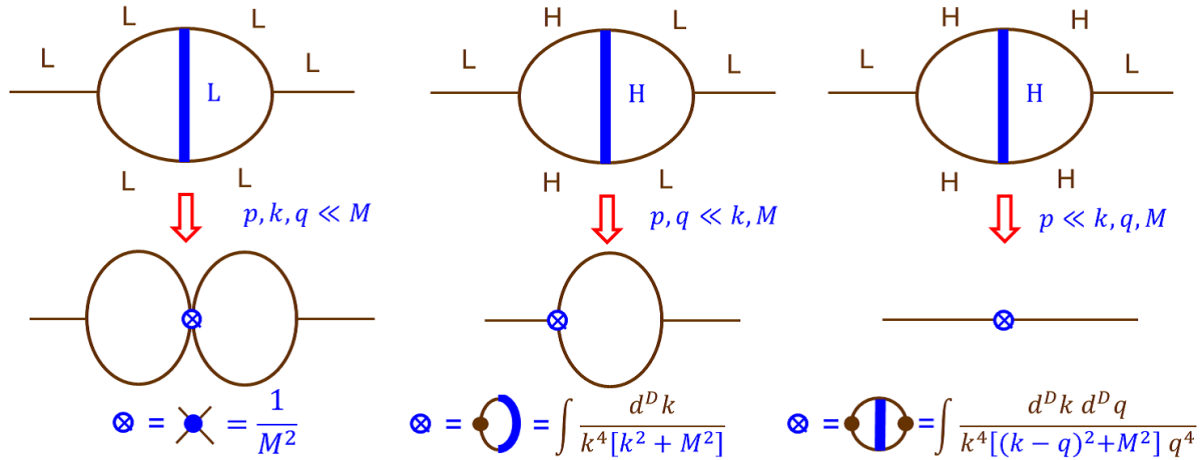


Figure 10: Diagrams showing procedure of the asymptotic expansion. The bottom line represent the Wilson coefficients of the leading-order effective vertices in respective regions.

In the region (H,L) we expand the propagator $1/(p-k)^2$ in p and the propagator $1/[(k-q)^2 + M^2]$ in q . In each term of the expansion, integral over k can be factorized, since p, q enter only the numerator of the integrand and can be pulled outside of the integral. This produces effective three-point vertices, which correspond to three-point interactions given by local operators. The leading term of this expansion is depicted in the middle part of the figure. Since high momenta flow through the k -loop, it is natural to expect that the loop effectively shrinks to a point.

In the region (H,H) we expand $1/(p-k)^2$ and $1/(p-q)^2$ in p . In this case, the whole integral over k and p can be factorized at each order of the expansion. Thus, each term can be regarded as an effective two-point interaction corresponding to a local operator. See the right-most part of the figure.

We may compute the same process in a low-energy EFT in which the massive particle has been integrated out. The asymptotic expansion of the diagram in the full theory obtained above can be interpreted as the computation in the EFT. The bottom-left diagram in Fig. 10 represents a two-loop computation of this process in the EFT with an insertion of a four-point vertex, which is generated at tree-level of the full theory. The factor $1/M^2$ below the diagram represents the Wilson coefficient of the leading-

order vertex in expansion in $1/M^2$. The bottom-middle diagram represents a one-loop computation of this process in the EFT with an insertion of a three-point vertex, which is generated at one-loop level in the full theory. The one-loop integral shown below the diagram represents the Wilson coefficient of the leading-order vertex in expansion in $1/M^2$. The bottom-right diagram represents a tree-level computation of this process in the EFT with an insertion of a two-point vertex, which is generated at two-loop level in the full theory. The corresponding leading-order Wilson coefficient is shown as a two-loop integral. Thus, the relevant operators and Wilson coefficients of EFT can be identified.

The Wilson coefficients, given by loop integrals in dimensional regularization, are particularly convenient in practical computations. They are homogeneous in a single dimensionful parameter M , which can be computed relatively easily. In contrast, if we adopt a cut-off regularization, usually it becomes much more difficult to evaluate the corresponding integrals (especially at higher loops), since more scales are involved.

3.5 Higher-loop integrals and multiple zeta values

In this subsection we explain developments and recent activities in analytic evaluations of higher-loop corrections. As already mentioned, a general algorithm for analytic evaluation has not been found yet and there are diverse on-going researches. In particular we focus on intersection with an area of research in mathematics on multiple zeta values (MZVs).

We start by looking at analytic expressions for multi-loop corrections to the anomalous magnetic moment of electron ($g_e - 2$) as an example:*

$$a_e(\text{QED}) = a_e^{(2)}\left(\frac{\alpha}{\pi}\right) + a_e^{(4)}\left(\frac{\alpha}{\pi}\right)^2 + a_e^{(6)}\left(\frac{\alpha}{\pi}\right)^3 + a_e^{(8)}\left(\frac{\alpha}{\pi}\right)^4 + a_e^{(10)}\left(\frac{\alpha}{\pi}\right)^5 + \dots, \quad (12)$$

$$a_e^{(2)} = \frac{1}{2}, \quad (13)$$

$$a_e^{(4)} = \frac{197}{144} + \frac{\pi^2}{12} + \frac{3}{4}\zeta(3) - \frac{\pi^2}{2}\ln 2, \quad (14)$$

$$a_e^{(6)} = \frac{83}{72}\pi^2\zeta(3) - \frac{215}{24}\zeta(5) + \frac{100}{3}\left(\text{Li}_4\left(\frac{1}{2}\right) + \frac{1}{24}\ln^4 2 - \frac{1}{24}\pi^2\ln^2 2\right) - \frac{239}{2160}\pi^4 \\ + \frac{139}{18}\zeta(3) - \frac{298}{9}\pi^2\ln 2 + \frac{17101}{810}\pi^2 + \frac{28259}{5184}, \quad (15)$$

where $\mathcal{O}(m_e/m_\mu)$ terms are omitted. Presently the corrections are known analytically up to three loops ($a_e^{(6)}$) [19] while they are known numerically up to five loops ($a_e^{(10)}$) [20]. The above expressions include a class of transcendental numbers, which can be

* Although it is a perturbative QED prediction, its analytic feature, in which we are interested, is similar to that of perturbative QCD predictions.

expressed as infinite sums:

$$\zeta(n) = \sum_{m=1}^{\infty} \frac{1}{m^n}, \quad \ln 2 = - \sum_{m=1}^{\infty} \frac{(-1)^m}{m}, \quad (16)$$

$$-2 \left(\text{Li}_4\left(\frac{1}{2}\right) + \frac{1}{24} \ln^4 2 - \frac{1}{24} \pi^2 \ln^2 2 \right) + \frac{\pi^4}{180} = \sum_{m>n>0} \frac{(-1)^{m+n}}{m^3 n}, \quad (17)$$

where $\zeta(x)$ and $\text{Li}_n(x) = \sum_{k=1}^{\infty} \frac{x^k}{k^n}$ denote the Riemann zeta function and polylogarithm, respectively. Note that, since $\zeta(2n)$ is proportional to π^{2n} for $n \in \mathbb{N}$, π^2 and π^4 in $a_e^{(2n)}$ can be regarded as this class of numbers (up to rational coefficients) as well.

A generalized MZV is defined by a nested sum

$$Z(\infty; a_1, a_2, \dots, a_N; \lambda_1, \lambda_2, \dots, \lambda_N) = \sum_{n_1 > n_2 > \dots > n_N > 0} \frac{\lambda_1^{n_1} \lambda_2^{n_2} \dots \lambda_N^{n_N}}{n_1^{a_1} n_2^{a_2} \dots n_N^{a_N}}, \quad (18)$$

where $a_i \in \mathbb{N}$ and $a_1 \geq 2$. In the case $\lambda_i \in \{1\}$ it is simply called a MZV; in the case $\lambda_i \in \{-1, 1\}$ it is called a sign-alternating Euler sum. We also consider the case that λ_i is a root of unity (e.g. $\lambda_i = e^{i\pi/3}$). In many classes of higher-loop computations, including the above example, these types of generalized MZVs appear in the analytic results.

Each generalized MZV also has a nested integral representation. By way of example,

$$\int_0^1 \frac{dx}{x} \int_0^x \frac{dy}{y - \alpha} \int_0^y \frac{dz}{z - \beta} = -Z\left(\infty; 2, 1; \frac{1}{\alpha}, \frac{\alpha}{\beta}\right), \quad (19)$$

which can be verified easily by rewriting the integrand as an infinite series expansion in y and z and integrating each term. As inferred from this example, in the case that λ_i 's are roots of unity, generally the nested integral representation has singularities of the integral variables at zero or at roots of unity. We will use this property below.

Hereafter, we refer to generalized MZV simply as MZV. The weight of a MZV is defined as the sum of the powers of the summation indices in the denominator: $w = a_1 + \dots + a_N$ for eq. (18). It turns out that various MZVs can be expressed by a small set of basis MZVs. More precisely, one may consider the vector space over \mathbb{Q} spanned by MZVs at each given weight, and the dimension of the vector space is much smaller

than the number of MZVs. For instance, since the relation $\sum_{m>n>0} \frac{1}{m^2 n} = \sum_{m=1}^{\infty} \frac{1}{m^3} = \zeta(3)$

holds, we find that, for $\lambda_i \in \{1\}$ and at weight three, the dimension is one, while there are two MZVs. In fact, in the case $\lambda_i \in \{1\}$, mathematicians have proven [21, 22, 23] that the dimension of the vector space at weight w is less than or equal to d_w , which is determined by a Fibonacci-type recursion relation

$$d_0 = 1, \quad d_1 = 0, \quad d_2 = 1, \quad d_w = d_{w-2} + d_{w-3} \quad (w \geq 3). \quad (20)$$

(The dimension is most likely to be equal to d_w .) Tab. 1 shows d_w and the number of

weight	w	0	1	2	3	4	5	6	7	8	9	10	11	12
dimension(?)	d_w	1	0	1	1	1	2	2	3	4	5	7	9	12
#(MZVs)	2^{w-2}	-	-	1	2	4	8	16	32	64	128	256	512	1024

Table 1: (Upper bound for) Dimension d_w of the vector space spanned by MZVs and the number of MZVs for a given weight w up to 12 and $\lambda_i \in \{1\}$.

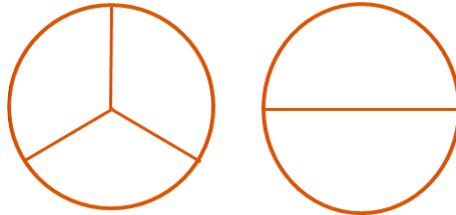


Figure 11: Diagrams which include MZVs with sixth roots of unity $\lambda_i = e^{in_i\pi/3}$. Each line corresponds to either a massive propagator with mass m or a massless propagator.

MZVs for weights up to 12. One sees that indeed MZVs can be expressed by a small set of basis. This fact allows us to obtain compact analytic expressions for higher-loop radiative corrections, although they originally stem from vast numbers of Feynman diagrams. Properties of MZVs can be explored using various non-trivial algebraic relations among them. In particular, empirically “shuffle relations” are known to be powerful in reducing MZVs to a smaller set (and probably provide maximal algebraic relations in the case $\lambda_i \in \{1\}$) [24].[†] It is stated that, by interpreting MZVs as periods of mixed motives, properties of MZVs can be understood from deeper viewpoints. Indeed mathematicians seem to observe deeper structures behind the world of MZVs.

Relations between topologies of Feynman diagrams and MZVs are the subjects of common interests for mathematicians and physicists; see e.g. [26, 27, 28]. Mathematicians may want to relate a topology, represented by a Feynman diagram, to MZVs as given by the value of the diagram. This may be used to characterize topologies if the relations are understood well. Physicists want to find a systematic way to relate a topology of a diagram to the value of the diagram when expressed in terms of MZVs. If this is achieved, we may find an efficient way to evaluate Feynman diagrams in terms of MZVs.

Below we discuss what kind of MZVs (in particular which λ_i 's) are associated with a diagram. Although no systematic argument exists up to now, we discuss some empirical aspects gained through experiences in explicit higher-loop computations. For instance, the diagrams shown in Fig. 11 are known to be expressed by MZVs with λ_i 's given by sixth roots of unity.

In general, λ_i 's are closely connected to singularities in a Feynman diagram, which are also closely tied to the topology of the diagram. Singularities contained in a Feynman

[†] We have recently found a new type of relations independent of the shuffle relations in the case λ_i 's are roots of unity [25].

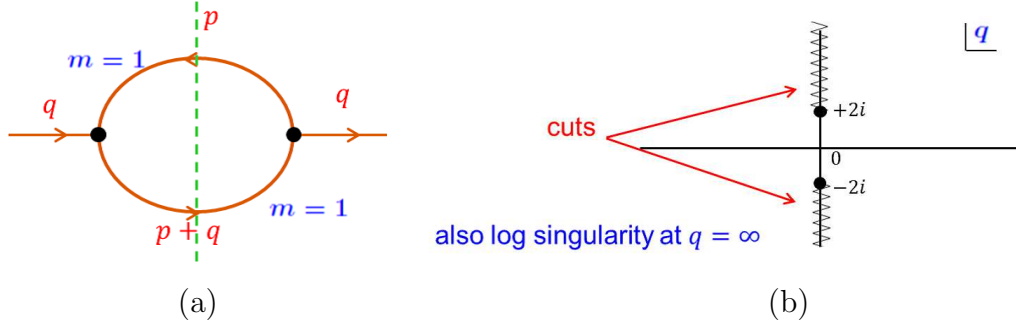


Figure 12: (a) Diagram for $I(q)$ defined in Eq. (21). The mass in the propagators is taken as $m = 1$. Imaginary part of $I(q)$ appears for $q^2 < -(2m)^2 = -4$ corresponding to the cut shown by the dashed line. (b) Analyticity of $I(q)$ in the complex q -plane.

diagram may be classified as follows:

- IR singularity, generated as external momenta are taken to zero.
- UV singularity, generated as external momenta are taken to infinity.
- Mass singularity, generated as the masses of internal particles are taken to zero.
- Threshold singularity, generated as the external energy crosses the threshold energy of an intermediate state.

In general overlaps of these types of singularities are included in a multiloop digram. There is no known systematic method to disentangle general overlapping singularities in such a way to cast them into MZVs (if this is possible at all).[‡] In simple cases this can be achieved, for instance, by iteratively applying the method of differential equation [29]; one can reduce a complicated diagram as integrals over simpler diagrams iteratively, and in the end as a combination of nested integrals, which can be converted to MZVs.

For illustration we consider a simple example. Consider a one-loop integral

$$I(q) = \int d^4p \frac{1}{(p^2 + 1)^2[(p + q)^2 + 1]} \propto \frac{1}{q^2 \sqrt{1 + 4/q^2}} \log \left(\frac{\sqrt{1 + 4/q^2} + 1}{\sqrt{1 + 4/q^2} - 1} \right). \quad (21)$$

The diagram is shown in Fig. 12(a), where the masses of internal lines are taken to be the same, $m = 1$. The power of one of the propagators is raised in order to make the integral well defined in four dimension.[§] Fig. 12(b) shows the analyticity of $I(q)$ in the complex q -plane. The square-root $\sqrt{1 + 4/q^2}$ generates branch points corresponding to the threshold singularities at $q = \pm 2im = \pm 2i$. (Note that we are working in Euclidean space-time.) There is also a logarithmic singularity at $q = \infty$, which can be regarded as a UV singularity, or alternatively as a mass singularity.

[‡] In numerical evaluations disentanglement of overlapping singularities is always possible in finite steps, using sector decomposition and the theorem on resolution of singularities [11].

[§] Powers of propagators are not essential in the following argument to identify λ_i of MZV.

We can express the second diagram of Fig. 11 as an integral over $I(q)$:

$$\int d^4q \frac{1}{(q^2 + 1)^2} I(q) \propto \text{Im} \left[\sum_{n=1}^{\infty} \frac{e^{i\pi n/3}}{n^2} \right], \quad (22)$$

where we raised the power of the propagator to make the integral well defined. All the lines of the diagram have equal masses, $m = 1$. On the left-hand-side, we can convert the integral to a one-dimensional integral over q . The square-root in $I(q)$ can be eliminated by an Euler transformation $x = \frac{1}{2}(1 + \sqrt{1 + 4/q^2})$. We may further express the logarithm as an integral of a rational function. In this way, one can convert the integral to a nested double integral of rational functions, which is in fact a MZV. The map of the singularities by the Euler transformation is given by

$$\{\pm i, \pm 2i, \infty\} \xrightarrow{x = \frac{1 + \sqrt{1 + 4/q^2}}{2}} \{e^{\pm\pi i/3}, -, (0, 1)\}. \quad (23)$$

The singularities at $\pm i$ are associated with the propagator $1/(q^2 + 1)^2$ attached to $I(q)$ and those at $\{\pm 2i, \infty\}$ are the ones associated with $I(q)$. The map is double-valued, and the singularities at $\pm 2i$ are mapped to regular points. Thus, we see that sixth-roots of unity are generated by this map from physical singularities in the diagram.

Empirically we observe similar mechanisms in relating physical singularities of a diagram to λ_i 's of MZVs, for instance, when conversion to MZVs is possible by the method of differential equation. Sometimes square-roots are involved at intermediate stages, and in simple cases all the square-roots can be eliminated by successive Euler transformations. Thus, the origins of λ_i 's are indeed attributed to physical singularities of diagrams in these cases.

3.6 Closing the first part: summary and benchmarks

Let us summarize the overview of perturbative QCD presented above. This is depicted schematically in Fig. 13. Higher-order corrections in purely perturbative predictions include uncertainties of order $(\Lambda_{\text{QCD}}/E)^n$ from IR renormalons. This is because higher-order corrections tend to be more sensitive to IR regions, which can effectively be represented by an increase of the strong coupling constant $\alpha_s(k)$ at IR. Using OPE within a Wilsonian EFT, one may separate UV and IR contributions. The former are incorporated into Wilson coefficients and the latter into non-perturbative matrix elements. In this formulation, only UV part of the higher-order corrections of the purely perturbative prediction is encoded in the Wilson coefficients, whereas uncertainties originating from IR renormalons are replaced by non-perturbative matrix elements. Hence, intrinsic uncertainties of perturbative expansions can be eliminated, and we obtain more accurate predictions as we compute higher-orders corrections (as far as non-perturbative matrix elements can be determined in some way). These frameworks have been known since long time, at least conceptually. In practice, however, higher-order computations based on

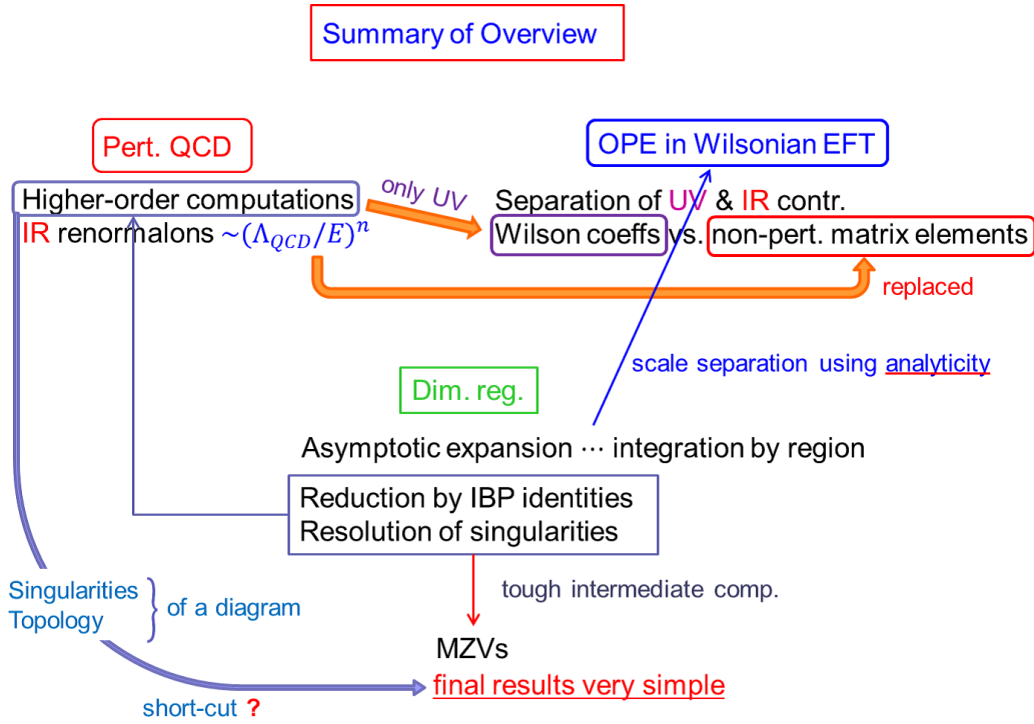


Figure 13: Schematic diagram showing mutual connections of the subjects covered in the overview given in Secs. 2 and 3.

EFTs had been quite difficult, since in earlier days they were formulated by introducing a cut-off in the integrals in an essential way.

Developments of perturbative QCD over the last few decades rely heavily on significant developments in computational technologies. In particular, dimensional regularization has been the theoretical basis for many important technological developments.

Asymptotic expansion of diagrams, or integration by regions, is a technique based on dimensional regularization and has provided a solid foundation to OPE of EFT. This technique enables computations of Wilson coefficients to high orders, since integrals can be cast into forms much easier to evaluate than ones with a cut-off. An important feature is that the scale separation is realized using analyticity of diagrams. A contour integral surrounding each singularity represents a contribution from the corresponding scale.

Furthermore, we explained a reduction of loop integrals using IBP identities, and discussed relation between singularities of Feynman diagrams and MZVs. These techniques are used in higher-loop computations. Essentially the computations are composed by processes of resolution of singularities in Feynman diagrams. As a general feature of these processes, the amount of calculation expands enormously at intermediate stages. On the other hand, final results tend to be compact, reflecting the nature of MZVs. This indicates that there may be a short-cut in finding final results, for instance by looking at singularities and topologies of diagrams.

Thus, dimensional regularization has brought in new computational methods as well

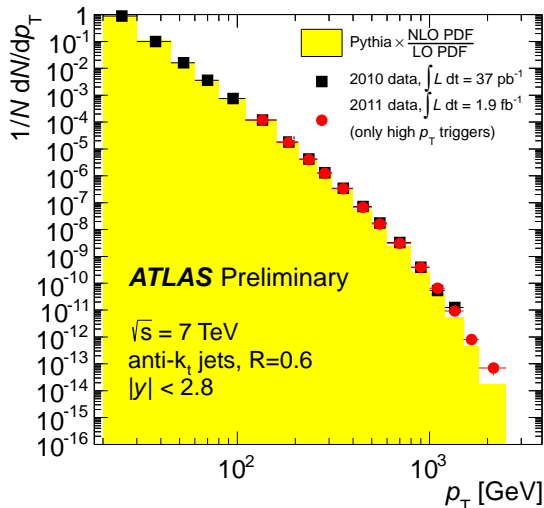


Figure 14: Jet P_T spectrum measured at the LHC experiment at $\sqrt{s} = 7$ TeV [30]. Observed inclusive jet P_T distribution (black dots) is compared to MC prediction (yellow histogram). The distribution is normalized to unity and only statistical uncertainties are included.

as viewpoints which are complementary and contrasting to those based on cut-off regularization. Fig. 13 displays a summary of the current status of perturbative QCD as seen from the author’s viewpoint.[¶] This sets up a general formulation of analyses. We should discuss physics using the formulation. As an example, we analyze heavy quarkonium systems in the second part of this paper.

To end the first part, it would be fruitful to note some of today’s benchmarks of perturbative QCD.

Universality

In the limit where the quark masses are neglected, QCD is a theory with a single scale Λ_{QCD} . It is remarkable that such a theory can explain physics phenomena over many orders of magnitude. Fig. 14 shows a comparison of experimental data and perturbative QCD prediction (in the sense of type (c) in Sec. 2.1) for the jet P_T spectrum at LHC. The theory prediction is predominantly determined by perturbative QCD. The current theoretical errors are typically order 10% to a few tens %. In the figure jet P_T ranges over two orders of magnitude (from 10 GeV to a few TeV), while the inclusive jet P_T distribution varies more than ten orders of magnitude! Although the relative accuracy of the prediction at each P_T is not so precise, it is quite impressive to observe a good agreement between the perturbative QCD prediction and experimental data for such a wide range of variation.

Precisions

Presently several parameters of the QCD Lagrangian are determined using perturba-

[¶] On-going active developments related to LHC physics are omitted.

tive QCD, combined with experimental data and results of lattice QCD computations, with the following accuracies [31]:

$$\alpha_s(M_Z) = 0.1184(7) \quad 0.6\% \text{ accuracy}, \quad (24)$$

$$\overline{m}_b = 4.18(3) \text{ GeV} \quad 0.8\% \text{ accuracy}, \quad (25)$$

$$\overline{m}_c = 1.275(25) \text{ GeV} \quad 2\% \text{ accuracy}, \quad (26)$$

$$\overline{m}_t = 160_{-4}^{+5} \text{ GeV} \quad 3\% \text{ accuracy } (\rightarrow 0.06\% \text{ at ILC}), \quad (27)$$

where $\alpha_s(M_Z)$ denotes the strong coupling constant in the modified minimal-subtraction ($\overline{\text{MS}}$) scheme, renormalized at the scale of the mass of the Z boson; \overline{m}_q denotes the $\overline{\text{MS}}$ mass (mass defined in the $\overline{\text{MS}}$ scheme) renormalized at the $\overline{\text{MS}}$ mass scale of a quark q .^{||} As can be seen, perturbative QCD is entering an era of high precision science.

4 Application to Heavy Quarkonium Systems

In this section we review application of perturbative QCD to heavy quarkonium systems with respect to the formulation discussed in Secs. 2 and 3. In particular we discuss (1) $\mathcal{O}(\Lambda_{\text{QCD}})$ physics in the heavy quark mass and interquark force, and (2) renormalization of Wilson coefficients at IR.

4.1 IR contributions in the static QCD potential

Let us first quote the current status of the static QCD potential. Fig. 15 shows the potential energy between two static color charges, which combine to color-singlet, as a function of the distance r between the charges. The units are scaled by the QCD scale in the $\overline{\text{MS}}$ scheme at three-loop order, $\Lambda_{\overline{\text{MS}}}^{3\text{-loop}}$ [42]. The NNNLO perturbative QCD prediction and lattice computations are compared. The three solid lines correspond to the perturbative predictions [33, 34] with scale choices* $\Lambda_{\overline{\text{MS}}}^{3\text{-loop}}/\mu = 0.14, 0.07$ and 0.035 . The data points represent lattice results by three different groups [35, 36, 37]. The number of quark flavor is set to zero in both computations. r_0 denotes the Sommer scale, which is interpreted as about 0.5 fm. Hence, the largest r in this figure is about

^{||} The current top quark mass $m_t = 173.34 \pm 0.76$ GeV [32] measured at Tevatron and LHC is theoretically not well defined. The measured mass corresponds to a parameter in MC simulations and its relation to the parameters of the QCD Lagrangian is unknown beyond order 1–2 GeV accuracy. By contrast, the $\overline{\text{MS}}$ mass is well defined and its relation to the parameters of the QCD Lagrangian is theoretically solid.

* It is customary to vary the renormalization scale μ by a factor 2 or 1/2 in estimating uncertainties of perturbative QCD predictions.

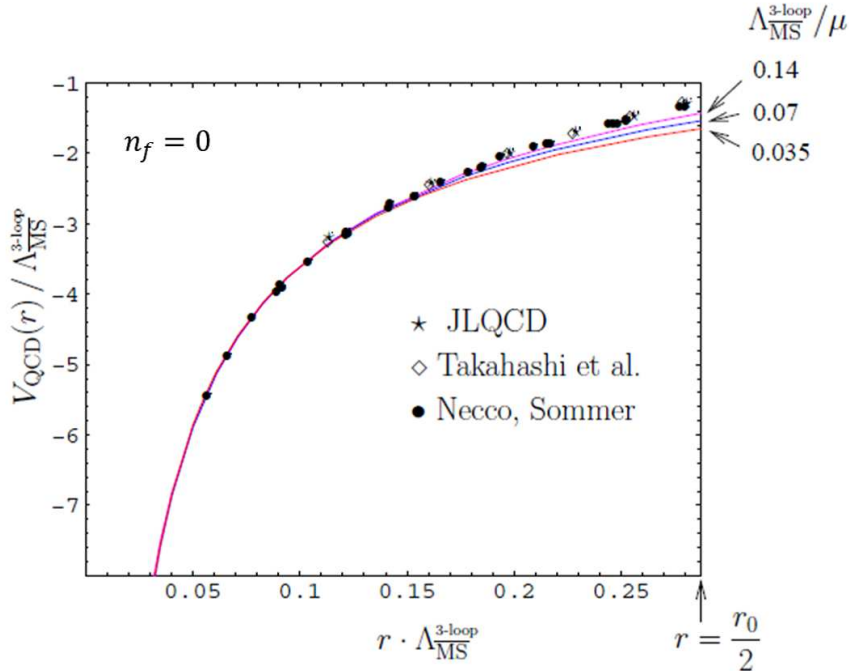


Figure 15: Static QCD potential as a function of the distance between the static charges r . Both axes are scaled by powers of $\Lambda_{\overline{\text{MS}}}^{3\text{-loop}}$. Solid lines represent NNNLO perturbative QCD predictions with different scale choices. Data points represent lattice computations by three different groups.

0.25 fm [$\approx (0.8 \text{ GeV})^{-1}$]. Since the relation between the lattice scale (r_0) and $\Lambda_{\overline{\text{MS}}}^{3\text{-loop}}$ is taken from other source, the only adjustable parameter in this comparison is an r -independent constant added to each potential, whose value is chosen such that all the potentials coincide at $r\Lambda_{\overline{\text{MS}}}^{3\text{-loop}} = 0.1$. We see a good agreement between the perturbative and lattice predictions in the displayed range.

To understand the nature of the perturbative prediction for the static potential $V_{\text{QCD}}(r)$, we first discuss the IR renormalons of $V_{\text{QCD}}(r)$. Since the perturbative prediction is more accurate at short distances, $r \ll \Lambda_{\text{QCD}}^{-1}$, we consider (naively) a short-distance expansion of $V_{\text{QCD}}(r)$:

$$V_{\text{QCD}}(r) \sim \frac{c_{-1}}{r} + c_0 + c_1 r + c_2 r^2 + \dots \quad (28)$$

This expansion in r is naive, in the sense that there must be a logarithmic correction (at least) to the Coulomb term $\sim 1/[r \log(\Lambda_{\text{QCD}} r)]$, as designated by the renormalization-group equation. From the computation of the bubble-chain diagrams in Fig. 16(a) IR

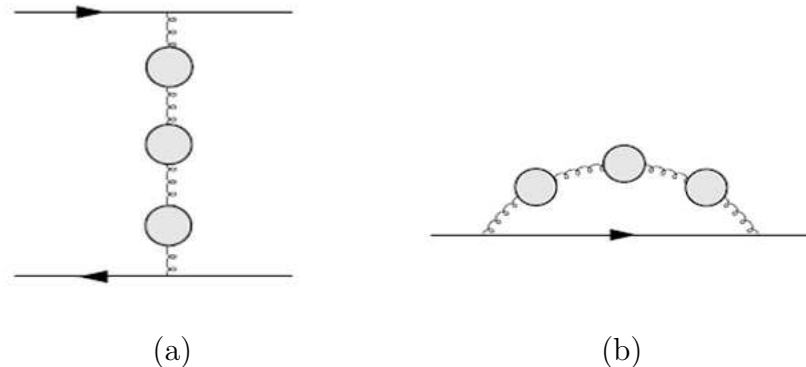


Figure 16: Bubble-chain diagrams contributing to (a) the static QCD potential and (b) the pole mass.

renormalons in the perturbative prediction for $V_{\text{QCD}}(r)$ can be estimated [38]; see Sec. 2.1. They arise in the form $\Lambda_{\text{QCD}}(\Lambda_{\text{QCD}} r)^P$. The leading uncertainty at $r \ll \Lambda_{\text{QCD}}^{-1}$ is included in the r -independent constant, while the next-to-leading uncertainty is included in the r^2 term:

$$c_0 \sim \mathcal{O}(\Lambda_{\text{QCD}}), \quad (29)$$

$$c_2 r^2 \sim \mathcal{O}(\Lambda_{\text{QCD}}^3 r^2). \quad (30)$$

The leading uncertainty can be eliminated in the following manner. Consider the total energy of a static quark pair defined by

$$E_{\text{tot}}(r) = 2m_{\text{pole}} + V_{\text{QCD}}(r). \quad (31)$$

We express the quark pole mass m_{pole} by the $\overline{\text{MS}}$ mass $\overline{m} \equiv m_{\overline{\text{MS}}}(m_{\overline{\text{MS}}})$ as

$$m_{\text{pole}} = \overline{m} (1 + d_1 \alpha_s + d_2 \alpha_s^2 + d_3 \alpha_s^3 + d_4 \alpha_s^4 + \dots). \quad (32)$$

Then, in the series expansion of $E_{\text{tot}}(r)$ in α_s , the leading IR renormalon contained in c_0 is canceled against the leading IR renormalon contained in m_{pole} , which is estimated from the diagrams in Fig. 16(b) [39, 40, 41]. The remaining largest renormalon of $E_{\text{tot}}(r)$ becomes order $\Lambda_{\text{QCD}}^3 r^2$ in $c_2 r^2$. As a result, uncertainties of the perturbative series for $E_{\text{tot}}(r)$ are much more suppressed at $r \ll \Lambda_{\text{QCD}}^{-1}$ as compared to those for $V_{\text{QCD}}(r)$, namely, the perturbative series for the former is much more convergent than that for the latter. This feature is shown in Figs. 17(a)(b). In the left figure the perturbative

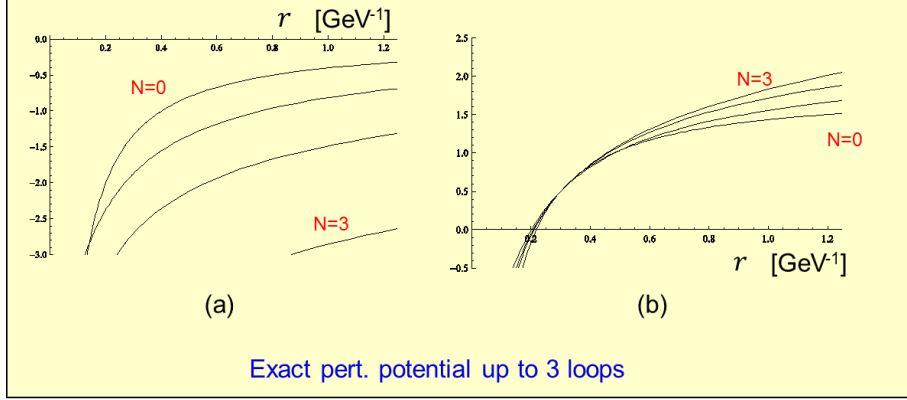


Figure 17: Comparisons of perturbative predictions of $V_{\text{QCD}}(r)$ up to $\mathcal{O}(\alpha_s^{N+1})$ for $N = 0, 1, 2$ and 3 , as they are [(a)], and after the leading renormalon is canceled by adding an r -independent constant to each potential such that it takes a common value at $r = 0.3 \text{ GeV}^{-1}$ [(b)].

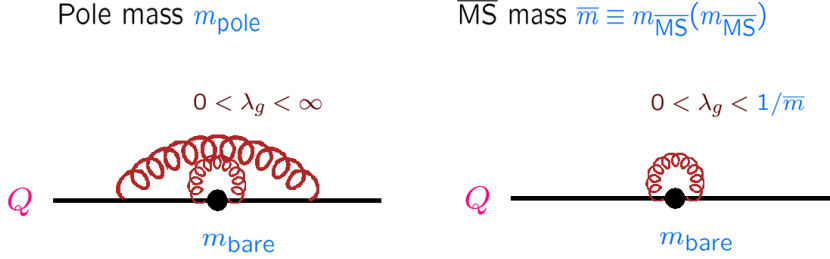


Figure 18: Schematic diagrams representing intuitive pictures of the pole mass and $\overline{\text{MS}}$ mass of a quark.

predictions for $V_{\text{QCD}}(r)$ up to $\mathcal{O}(\alpha_s^{N+1})$ are shown ($N = 0, 1, 2$ and 3). As we increase the order, there are large, almost constant shifts downwards, which make convergence of the perturbative series very poor in the displayed range of r . In the right figure, we effectively cancel the renormalon in c_0 by adding an r -independent constant to each potential such that it takes a common value at $r = 0.3 \text{ GeV}^{-1}$.[†] As can be seen, the predictions in Fig. 17(b) is much more convergent. Furthermore, we note that the potential becomes steeper as we include higher-order corrections [43]. This is a desirable tendency for the potential to approach the correct shape by inclusion of higher-order corrections. If we estimate the perturbative series of the potential by the bubble-chain contributions and make similar plots, they look qualitatively the same as Figs. 17(a)(b). Thus, the renormalon estimates are indeed good approximations for the static potential.

Let us explain physical interpretations of the quark pole mass and $\overline{\text{MS}}$ mass. See Fig. 18. The pole mass m_{pole} is defined as the position of the pole of a quark full propagator defined in perturbation theory. It is equivalent to the self-energy of a quark in its rest frame. Since a quark has color, gluons with arbitrarily long wave-lengths

[†] Since d_4 of eq. (32) is unknown at present, we cannot display $E_{\text{tot}}(r)$ at $\mathcal{O}(\alpha_s^4)$. We observe a qualitatively similar feature as in Fig. 17(b) if we plot $E_{\text{tot}}(r)$ up to $\mathcal{O}(\alpha_s^3)$.

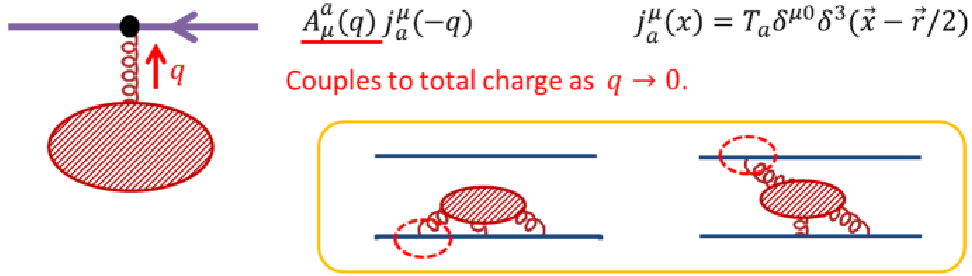


Figure 19: As a general feature of gauge theory, a gluon, which couples to static currents $j_a^\mu \propto \delta^{\mu 0}$, couples to the total charge of the system in the IR limit, $q \rightarrow 0$. Diagrammatically both self-energy and potential-energy type diagrams are needed for realizing this feature, hence, for a color-singlet system, a cancellation takes place between the two types of diagrams.

(small momenta) can couple to the quark and contribute to the self-energy. On the other hand, the $\overline{\text{MS}}$ mass \overline{m} is defined as the contributions to the quark self-energy from gluons with wave-lengths smaller than $1/\overline{m}$. Hence, the difference between m_{pole} and \overline{m} is given by the contributions to the quark self-energy from IR gluons (wave-lengths larger than $1/\overline{m}$). Twice of this difference corresponds to the additional terms in $E_{\text{tot}}(r)$ [twice of eq. (32) minus $2\overline{m}$].

The cancellation of IR contributions in $E_{\text{tot}}(r)$ is a general property of gauge theory, which holds beyond the estimates by the bubble-chain diagrams. In fact, a gluon, which couples to static currents $j_a^\mu \propto \delta^{\mu 0}$ via minimal coupling $A_\mu^a j_a^\mu$, couples to the total charge of the system $Q_a^{\text{tot}} = \sum_i j_{a,i}^0(q=0)$ ($i = Q, \bar{Q}$) in the zero momentum limit $q \rightarrow 0$. Namely, an IR gluon decouples from the color-singlet system. Diagrammatically an IR gluon observes the total charge of the system when both self-energy diagrams[‡] and potential-energy diagrams are taken into account. This means that a cancellation takes place between these two types of diagrams, see Fig. 19. In perturbative QCD, convergence of perturbative series become worse as contributions from IR gluons grow. Oppositely, after cancellation of IR contributions, convergence of perturbative predictions improve. This can be considered as a general property of a gauge theory which is strongly interacting at IR.

Thus, the dominant IR contributions to $V_{\text{QCD}}(r)$ are contained in the c_0 and $c_2 r^2$ terms in Eq. (28). The renormalon in c_0 is canceled against the pole mass in $E_{\text{tot}}(r)$. On the other hand, the renormalon in $c_2 r^2$ is replaced by a non-perturbative matrix element in OPE of $V_{\text{QCD}}(r)$ within an EFT “potential-NRQCD” [44], as explained below.

The potential-NRQCD [6] is an EFT for describing interactions between IR gluons and heavy quark-antiquark ($Q\bar{Q}$) bound-states. Since Q and \bar{Q} are heavy, the size r of a bound-state is small $r < \Lambda_{\text{QCD}}^{-1}$. In this EFT, the leading interaction between a color-

[‡] In the large mass limit contributions from IR region to the pole mass approximate IR contributions to the self-energy of a static charge.

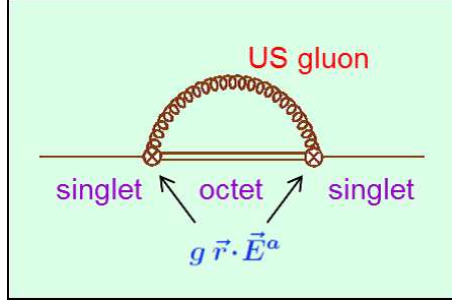


Figure 20: Diagram in potential-NRQCD EFT which contributes to $E_{\text{tot}}(r)$. The single and double straight lines represent the singlet and octet $Q\bar{Q}$ states, respectively. “Ultra-soft (US) gluon” represents an IR gluon with energy appropriate for transitions between different $Q\bar{Q}$ states.

singlet $Q\bar{Q}$ state and IR gluon in multipole expansion in \vec{r} is a dipole-type interaction $\vec{r} \cdot \vec{E}^a$, where the r^0 coupling with the total charge vanishes due to the color-singlet nature of the $Q\bar{Q}$ state. Hence, the leading contribution to the energy of $Q\bar{Q}$ is expressed in terms of a matrix element[§]

$$\langle \vec{r} \cdot \vec{E}^a(t) \vec{r} \cdot \vec{E}^b(0) \rangle. \quad (34)$$

It contains the dipole interaction twice, since the gluon emitted from the $Q\bar{Q}$ bound-state needs to be reabsorbed; see Fig. 20. Thus, it is proportional to r^2 and in fact has a form which exactly matches to replace the order $\Lambda_{\text{QCD}}^3 r^2$ renormalon in $c_2 r^2$ [44, 45]. This exemplifies the relation between IR renormalons and non-perturbative matrix elements as explained in Sec. 3.2.

Note that there are no IR contributions to the $c_{-1} r^{-1}$ and $c_1 r$ terms in Eq. (28) by IR renormalons or by non-perturbative matrix elements in OPE of potential-NRQCD. Then, it is logically expected that the $c_{-1} r^{-1}$ and $c_1 r$ terms are dominated by UV contributions.[¶] In the next subsection, we answer to the question “What are the UV contributions to $V_{\text{QCD}}(r)$?”

[§] More precisely the non-perturbative contribution is given as a non-local gluon condensate

$$V_{\text{US}}(r) = -\frac{ig_S^2}{6} \int_0^\infty dt e^{-i\Delta V(r)t} \langle 0 | \vec{r} \cdot \vec{E}^a(t) \varphi_{\text{adj}}(t, 0)^{ab} \vec{r} \cdot \vec{E}^b(0) | 0 \rangle, \quad (33)$$

where $\Delta V(r)$ denotes the difference between the octet and singlet potentials, and $\varphi_{\text{adj}}(t, 0)^{ab}$ represents a color flux spanned between the coordinates $(0, \vec{0})$ and $(t, \vec{0})$. $V_{\text{US}}(r)$ reduces to the local gluon condensate $\sim r^3 \langle G_{\mu\nu}^a(0)^2 \rangle$ at very small r ($\ll \Delta V(r)^{-1}$), which lies outside the range of r considered here. See [44] for details.

[¶] After canceling the renormalons, the r independent term of $E_{\text{tot}}(r)$ is also dominated by UV contribution.

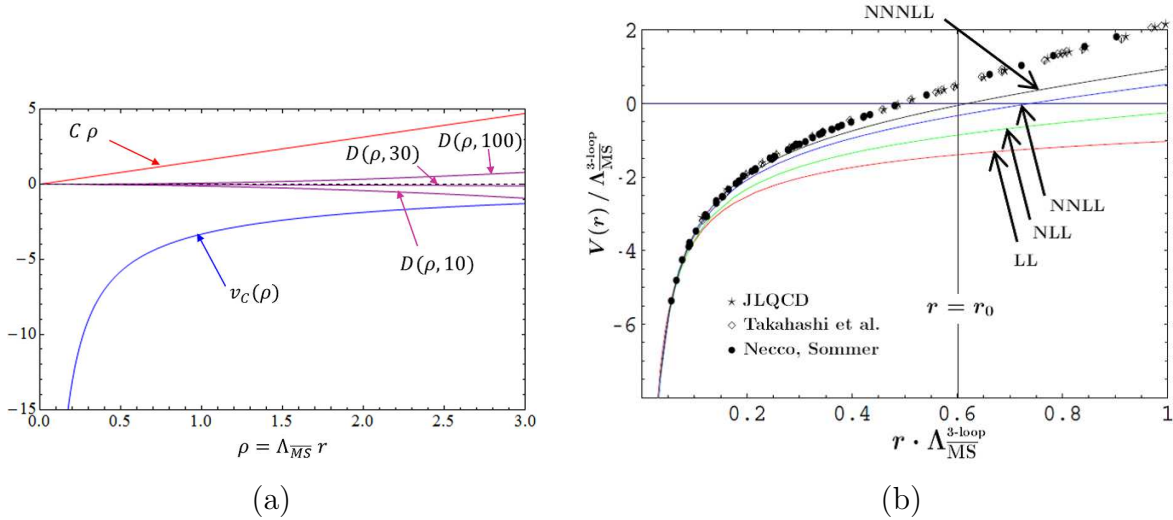


Figure 21: (a) ‘‘Coulomb,’’ linear and $\mathcal{O}(\Lambda_{\text{QCD}}^3 r^2)$ parts of Eq. (35) in the LL approximation. See [46, 47] for details. (b) Comparison of lattice computations [35, 36, 37] of $V_{\text{QCD}}(r)$ and $V_C(r) + \sigma r$. Solid lines represent $V_C(r) + \sigma r$, defined by Eqs. (37) and (38), at different orders of log resummations.

4.2 UV contributions as a ‘‘Coulomb+linear’’ potential

In this subsection we show that the UV contribution to $V_{\text{QCD}}(r)$ in perturbative QCD takes a ‘‘Coulomb+linear’’ form, after resummation of logarithms [46, 45, 47]. Namely, the perturbative prediction can be cast into the form

$$V_{\text{QCD}}(r) = \underbrace{V_C(r)}_{r^{-1}} + \underbrace{\text{const.}}_{r^0} + \underbrace{\sigma r}_{r^1} + \underbrace{\mathcal{O}(\Lambda_{\text{QCD}}^3 r^2)}_{r^2} \quad \text{at } r \lesssim \Lambda_{\text{QCD}}^{-1}. \quad (35)$$

We first show the results and afterwards explain how they can be derived.

Fig. 21(a) shows each part of the above decomposition of the potential in the case that leading-logarithms (LL) are resummed. $v_C(\rho)$ and $C\rho$ correspond to the ‘‘Coulomb’’ and linear terms, respectively. Differences among $D(\rho, N)$ ’s represent the level of uncertainties induced by the $\mathcal{O}(\Lambda_{\text{QCD}}^3 r^2)$ renormalon. Here and hereafter, the r -independent constant is neglected. The figure shows that the LL potential is approximated well by the ‘‘Coulomb+linear’’ potential $V_C(r) + \sigma r$ in the range $r \lesssim \Lambda_{\overline{MS}}^{-1}$, since the $\mathcal{O}(\Lambda_{\text{QCD}}^3 r^2)$ uncertainties are not significant.

Fig. 21(b) shows a comparison of lattice data and $V_C(r) + \sigma r$ in different orders of log resummations. As can be seen, with increasing order, the range where the perturbative prediction agrees with the lattice data extends to larger r . These predictions for $V_C(r) + \sigma r$ are expressed by the parameters of perturbative QCD. For instance, the coefficient of the linear potential at NLL is given by

$$\sigma_{\text{NLL}} = \frac{2\pi C_F}{\beta_0} \left(\Lambda_{\overline{MS}}^{2\text{-loop}} \right)^2 \frac{e^{-\delta}}{\Gamma(1+\delta)} \left[1 + \frac{a_1}{\beta_0} \delta^{-1-\delta} e^\delta \gamma(1+\delta, \delta) \right], \quad (36)$$

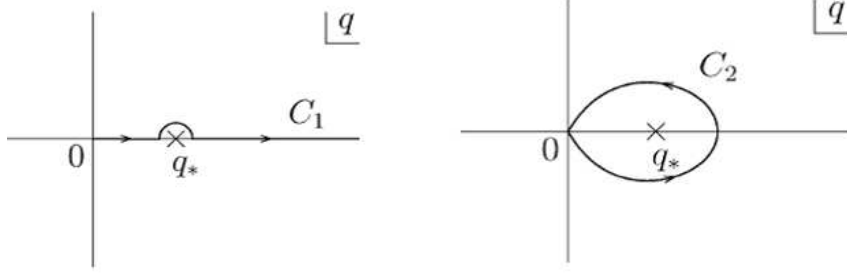


Figure 22: The contours C_1 and C_2 of integrals in Eqs. (37) and (38).

where $C_F = 4/3$ is the Casimir operator for the fundamental representation, and $\delta = \beta_1/\beta_0^2$; see [46, 47] for details.

The formulas for $V_C(r)$ and σr are given as contour integrals in the complex q -plane as follows:

$$V_C(r) = -\frac{C_F}{\pi i} \int_{C_2} dq \frac{\alpha_V(q)}{qr} - \frac{2C_F}{\pi} \text{Im} \int_{C_1} dq \frac{e^{iqr}}{qr} \alpha_V(q), \quad (37)$$

$$\sigma = \frac{C_F}{2\pi i} \int_{C_2} dq q \alpha_V(q). \quad (38)$$

The contours C_1 and C_2 are shown in Fig. 22. Here, the V -scheme coupling constant $\alpha_V(q)$ is defined from the Fourier transform of the potential by

$$V_{\text{QCD}}(r) = \int \frac{d^3\vec{q}}{(2\pi)^3} \left[-4\pi C_F \frac{\alpha_V(q)}{q^2} \right] e^{i\vec{q}\cdot\vec{r}} \quad ; \quad q = |\vec{q}|, \quad (39)$$

and can be computed in perturbative QCD.

In the case of LL approximation,

$$\alpha_V(q) = \frac{2\pi}{\beta_0 \log(q/\Lambda_{\overline{\text{MS}}}^{1\text{-loop}})} \quad (40)$$

coincides with the one-loop running coupling constant. The ‘‘Coulomb’’ potential $V_C(r)$ is easily computed numerically using the above formula, while its asymptotic behavior can be extracted analytically:

$$V_C^{(\text{LL})}(r) \rightarrow \begin{cases} -\frac{2\pi C_F}{\beta_0} \frac{1}{r \left| \log(\Lambda_{\overline{\text{MS}}}^{1\text{-loop}} r) \right|}, & r \rightarrow 0, \\ -\frac{4\pi C_F}{\beta_0 r}, & r \rightarrow \infty. \end{cases} \quad (41)$$

At short-distance it tends to a Coulomb potential with the correct logarithmic correction as determined by the RG equation; at large-distance, it approaches a Coulomb potential;

see Fig. 21(a). On the other hand, the coefficient of the linear potential can be computed analytically using the Cauchy theorem:

$$\sigma_{\text{LL}} = \frac{2\pi C_F}{\beta_0} \left(\Lambda_{\overline{\text{MS}}}^{1\text{-loop}} \right)^2. \quad (42)$$

To clarify the nature of $V_C(r) + \sigma r$, we compare it with the UV contribution to $V_{\text{QCD}}(r)$, defined as a Wilson coefficient in potential-NRQCD. Note that this EFT is valid in the case $r^{-1} \gg \mu_f \gg \Lambda_{\text{QCD}}$, where physical modes above the factorization scale μ_f have been integrated out. The relevant Wilson coefficient can be defined (in a hard cut-off scheme) as

$$V_{\text{UV}}(r; \mu_f) = \int_{q > \mu_f} \frac{d^3 \vec{q}}{(2\pi)^3} \left[-4\pi C_F \frac{\alpha_V(q)}{q^2} \right] e^{i\vec{q}\cdot\vec{r}}. \quad (43)$$

Since $\mu_f \gg \Lambda_{\text{QCD}}$, within the integral region $q > \mu_f$, $\alpha_V(q)$ can be computed accurately in perturbative QCD. In particular, V_{UV} is shown to be free of IR renormalons (in the estimate by the bubble-chain diagrams). V_{UV} represents the leading UV contribution to the static potential.^{||}

It can be proven that

$$V_{\text{UV}}(r; \mu_f) - [V_C(r) + \sigma r] = \text{const.} + \mathcal{O}(\mu_f^3 r^2). \quad (44)$$

This shows that, in perturbative QCD, the ‘‘Coulomb’’ and linear parts of $V_{\text{QCD}}(r)$ are determined by UV contributions and independent of the factorization scale μ_f .

$V_C(r) + \sigma r$ represents the ‘‘Coulomb’’ and linear parts of $V_{\text{QCD}}(r)$ in perturbative QCD by Eq. (35), and V_{UV} represents the UV contribution to $V_{\text{QCD}}(r)$. The above relation shows that there are no Coulomb or linear potential in the difference (at $r \ll \mu_f^{-1}$), namely they are included in the UV contribution. It is probably not surprising that the ‘‘Coulomb’’ potential arises from the UV contribution, since singular behavior as $r \rightarrow 0$ can only stem from the short-wave length modes $\lambda < r$ of gluons exchanged between the color-singlet pair Q and \bar{Q} . It would be surprising, however, that even the linear potential is a short-distance contribution. The above relation also shows that, since $V_C(r) + \sigma r$ is independent of μ_f , the ‘‘Coulomb’’ and linear potentials contained in V_{UV} are insensitive to the IR cut-off of eq. (43). In this sense, they are genuinely UV in nature. It is consistent, since if we raise μ_f in V_{UV} , μ_f -dependent part (an IR part) of V_{UV} should be compensated by IR operators in the EFT, but there are no IR operators which can absorb the r -dependences of $V_C(r)$ and σr .

The proof of Eq. (44) is given in the Appendix, which is fairly easy to understand. An essential point of the proof is that contributions from the IR scale of order Λ_{QCD}

^{||} In OPE in the form of Eq. (5), P should be identified with r^{-1} , and the matrix element multiplying the Wilson coefficient V_{UV} is $1 = \langle 0|0 \rangle = \langle S|S^\dagger S|S \rangle$, where S and $|S \rangle$ denote the field operator and the state vector of the color-singlet bound-state, respectively.

are given as contour integrals near the singularity of $\alpha_V(q)$ which arises as a result of resummation of logarithms. We can then separate the IR contributions from $V_{\text{QCD}}(r)$. This is in parallel to the argument given in Sec. 3.4, that contributions from different scales can be separated as contour integrals surrounding the corresponding singularities in a Feynman diagram. The difference is that at each order of perturbation we cannot see a singularity corresponding to the scale Λ_{QCD} , as it arises only after resummation of logarithms. Nevertheless, it should be noted that, as we saw in Sec. 3.1, inclusion of the higher-order corrections approximate to the resummed contribution, and sensitivity to the Λ_{QCD} scale becomes apparent gradually in perturbation theory even without a log resummation.

At this stage we stress the need for the IR renormalization of the Wilson coefficient $V_{\text{UV}}(r)$. Eq. (43) corresponds to introducing a hard cut-off to define a Wilsonian EFT. On the other hand, as we explained, the modern way to define an EFT is to separate scales by using asymptotic expansion in dimensional regularization. In this case, separation of IR contributions is non-trivial, since the IR scale Λ_{QCD} does not appear at any fixed-order of the perturbative expansion. In fact, one can show that the bare Wilson coefficient $V_{\text{UV}}(r)$ defined in dimensional regularization in EFT coincides with $V_{\text{QCD}}(r)$ in perturbative QCD to all orders in perturbative expansion. Therefore, this $V_{\text{UV}}(r)$ includes uncertainties by IR renormalons. It means that one needs to explicitly renormalize $V_{\text{UV}}(r)$ at IR by subtracting IR contributions in some prescription.** One way is to subtract an estimate of contributions from IR renormalons at each order of perturbative expansion [48]. The other method is the one we advocate above [47]: resum logarithms first, identify the IR singularity corresponding to the Λ_{QCD} scale in the resummed contribution, and separate its contribution by a prescription similar to the asymptotic expansion; in this way we can subtract the IR sensitive parts and renormalize them into the pole mass and non-perturbative matrix element; as a result we obtain $V_C(r) + \sigma r$ as a renormalized Wilson coefficient. Both prescriptions lead to similar results numerically, but the consequences are probably easier to interpret in the latter method.

There are two ways to derive the formulas for $V_C(r)$ and σr , Eqs. (37) and (38). One way is along the line of proof in the Appendix. In this way, $V_C(r) + \sigma r$ can be related to the perturbative evaluation of the Wilson coefficient V_{UV} after log resummation. The other way is to extract $V_C(r) + \sigma r$ from the perturbative series of $V_{\text{QCD}}(r)$. It can be shown that, while the perturbative series is converging (i.e., for $n < n_0$ of Sec. 3.1), the sum of the series approaches $V_C(r) + \sigma r$ up to an order $\Lambda_{\text{QCD}}^3 r^2$ uncertainty.

4.3 Implication and physical interpretation

Using $V_C(r) + \sigma r$ thus obtained, we can compute the total energy of a static $Q\bar{Q}$ pair as

$$E_{\text{tot}}(r) = 2\bar{m} + \text{const.} + V_C(r) + \sigma r + \mathcal{O}(\Lambda_{\text{QCD}}^3 r^2), \quad (45)$$

** This is a demerit of using asymptotic expansion for scale separation in perturbative QCD. It is not needed in construction of an EFT using a hard cut-off.

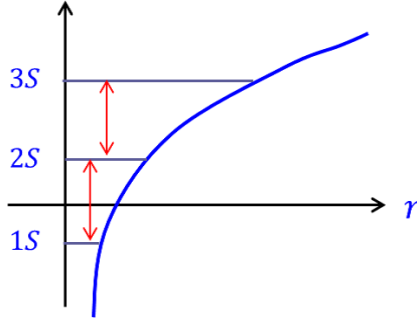


Figure 23: A schematic diagram showing the energy levels of the Hamiltonian Eq. (46). The level spacings are order $\Lambda_{\text{QCD}}(\Lambda_{\text{QCD}}/m)^{1/3}$ if they are predominantly determined by the linear part σr of the potential.

where the r -independent part is also UV dominant and accurately predictable. In principle, the $\mathcal{O}(\Lambda_{\text{QCD}}^3 r^2)$ uncertainty can be replaced by the non-perturbative matrix element in OPE. However, there has been no direct evaluation of the matrix element so far; it is only estimated to be small from a comparison of the potential to lattice data; see Figs. 15 and 21(b). The spectrum of a heavy quarkonium system, such as bottomonium or (would-be) toponium, can be computed roughly as the energy eigenvalues of the quantum mechanical Hamiltonian

$$H = \frac{\vec{p}^2}{2m_{\text{pole}}} + E_{\text{tot}}(r). \quad (46)$$

(More accurate prediction is possible using the potential-NRQCD framework. Currently the spectrum is known up to NNNLO [49].)

A linear potential of order $\Lambda_{\text{QCD}}^2 r$ generates level spacings between different S -states of order $\Lambda_{\text{QCD}}(\Lambda_{\text{QCD}}/m)^{1/3}$. On the other hand, a Coulomb potential $\sim -\alpha_s/r$ generates level spacings of order $\alpha_s^2 m$. For the bottomonium states, the linear potential is estimated to be comparable to or more important than the Coulomb potential in generating these level spacings, whereas for the toponium states, the Coulomb potential by far dominates over the linear potential. Thus, a major part of the perturbative QCD predictions for the level spacings between different bottomonium S -states is order $\Lambda_{\text{QCD}}(\Lambda_{\text{QCD}}/m)^{1/3}$. See Fig. 23.

We may develop a microscopic understanding on the composition of the energy of a bottomonium state based on perturbative QCD. According to the discussion in Sec. 4.1, infrared gluons decouple in the computation of the energy of a bottomonium state X . The energy consists of the self-energies of b and \bar{b} and the potential energy between b and \bar{b} , where gluons whose wave-lengths are smaller than the bound-state size a_X contribute. At IR the sum of the self-energies and the potential energy cancel. On the other hand,

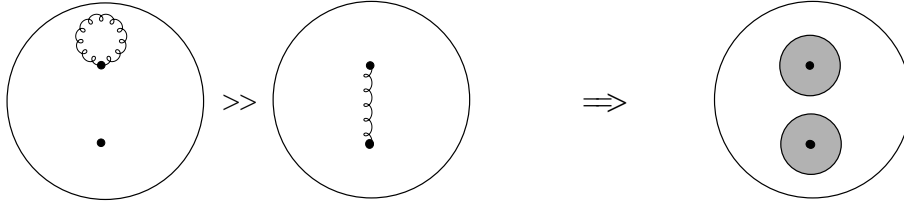


Figure 24: The total energy of a heavy quarkonium state is carried by the $\overline{\text{MS}}$ masses of quark and antiquark and by the gluons inside the bound-state. In the latter contributions the self-energies of quark and antiquark dominate over the potential energy between the two particles.

at UV, the potential energy quickly dumps due to the rapid oscillation factor e^{iqr} for large q in the potential energy. It means that the major contribution to the bottomonium energy comes from the region (in momentum space) $1/a_X \lesssim q \lesssim \overline{m}_b$ of the self-energy corrections of b and \bar{b} , apart from the constant contribution $2\overline{m}_b$. See Fig. 24.

In fact, the composition of the energy in momentum space can be expressed approximately as [50]

$$E_X \simeq 2\overline{m}_b + \frac{2C_F}{\pi} \int_0^{\overline{m}_b} dq \alpha_s(q) f_X(q), \quad (47)$$

where $f_X(q)$ is a support function constructed from the wave-function of the bound-state X , which is roughly unity in the region $1/a_X \lesssim q \lesssim \overline{m}_b$; see Fig. 25(a).

A characteristic feature of the bottomonium spectrum in comparison to the Coulomb spectrum is that the level spacings among the bottomonium excited states are much wider than those of the Coulomb spectrum. The level spacings of the Coulomb spectrum decrease quickly for higher levels. The difference from the Coulomb spectrum results from the linear rise of the potential. See Figs. 23 and 25(b).

The size a_X of the state X becomes larger for higher excited states. Then gluons with longer wave-lengths can contribute to the energy of X . Positive contributions to the self-energies increase rapidly since interactions of IR gluons become stronger by the running of the coupling constant. In Fig. 25(a) also $\alpha_s(q)$ is shown. We see that as the state varies from $X = 1S$ to $3S$, the coupling $\alpha_s(q)$, close to the dumping scale of $f_X(q)$, grows rapidly. According to Eq. (47), as the integral region extends down to smaller q , the self-energy contributions grow rapidly in comparison to the non-running case. (Note that the non-running case corresponds to the Coulomb spectrum.) The self-energies push up the energy levels of the excited states considerably and widen the level spacings among the excited states as compared to the Coulomb case.

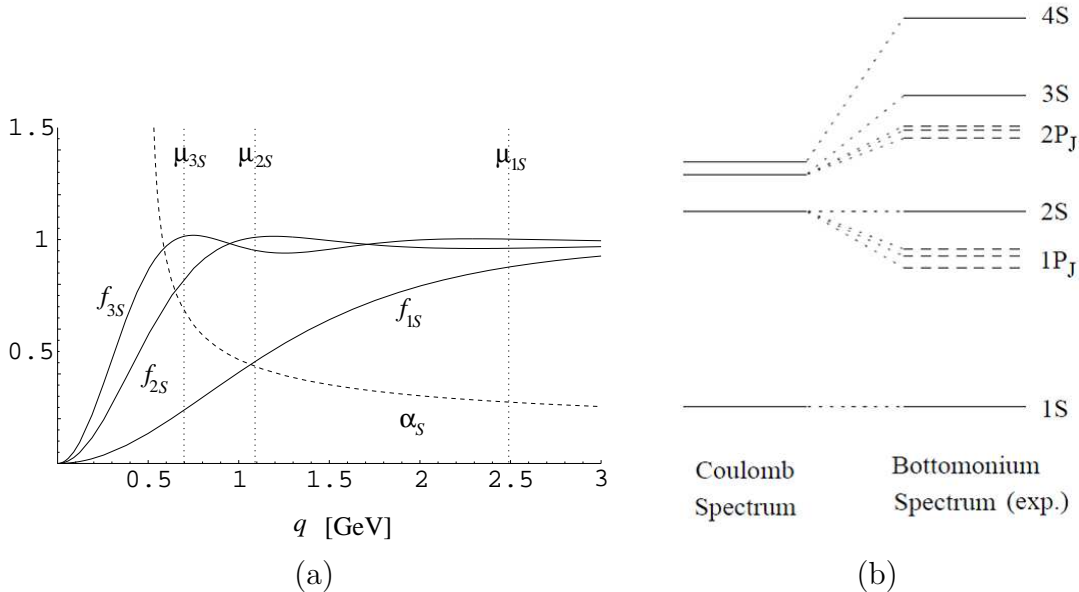


Figure 25: (a) The support functions $f_X(q)$ used to express the energy of the bottomonium state X in Eq. (47) for $X = 1S, 2S$ and $3S$ [50]. The running coupling constant $\alpha_s(q)$ close to the dumping scale of $f_X(q)$ grows rapidly as X varies from the $1S$ to $3S$ states. (b) Comparison of the Coulomb spectrum and observed bottomonium spectrum. The Coulomb spectrum is scaled such that the $1S$ - $2S$ level spacing coincides with that of the bottomonium spectrum.

Hence, we may draw the following qualitative pictures for the energies of the bottomonium states [50]:

- (I) The energy of a bottomonium state mainly consists of (i) the \overline{MS} masses of b and \bar{b} , and (ii) contributions to the self-energies of b and \bar{b} from gluons with wavelengths $1/\overline{m} \lesssim \lambda \lesssim a_X$. The latter contributions may be regarded as the difference between the (state-dependent) constituent quark masses and the current quark masses.
- (II) The energy levels between excited states are widely separated as compared to the Coulomb spectrum. This is because the self-energy contributions (from $1/\overline{m} \lesssim \lambda \lesssim a_X$) grow rapidly as the physical size a_X of the bound-state increases.

We conjecture that the conventional picture, that the mass of a light hadron consists of the constituent quark masses, can be viewed as an extrapolation of picture (I), although it lies outside the validity range of perturbative QCD.

The predictions of the bottomonium spectrum in perturbative QCD and their detailed quantitative analyses can be found in [49].

4.4 Lessons drawn from the analysis of heavy quarkonium states

There are lessons that can be drawn from the analysis of the heavy quarkonium states and static potential, which may be applicable in more general contexts.

- (1) One should carefully examine, from which power of $\Lambda_{\text{QCD}} = \mu \exp\left[-\frac{2\pi}{\beta_0\alpha_s(\mu)}\right]$ non-perturbative contributions start, and to which extent perturbative QCD is predictable (as we approach from the short-distance region).

It is a priori not obvious that the $\Lambda_{\text{QCD}}^2 r$ potential is dominated by UV contribution and predictable within perturbative QCD, while the $\Lambda_{\text{QCD}}^3 r^2$ potential is IR dominated and unpredictable in perturbative QCD. It can be clarified by the combined analyses of IR renormalons, OPE in Wilsonian EFT, and separation of IR contributions by log resummations and contour integrals.

- (2) Necessity of renormalization of Wilson coefficients at IR.

IR renormalization of Wilson coefficients needs to be performed *by hand*, in a modern framework of EFT which uses scale separation in dimensional regularization. This is because, identification of contributions from the Λ_{QCD} scale is not automatic at each order of perturbative expansion. One could inflate uncertainties of predictions if this prescription is not carried out properly.

In the application of perturbative QCD to the heavy quarkonium states, it is intriguing to see mutual connections between the running of $\alpha_s(q)$, the linear rise $\sim \Lambda_{\text{QCD}}^2 r$ of the interquark potential, and the quark self-energy of order $\Lambda_{\text{QCD}}(\Lambda_{\text{QCD}}/m)^{1/3}$ which resembles the constituent quark mass. The relations are made quantitative in the perturbative regime of QCD, $r \lesssim \Lambda_{\text{QCD}}^{-1}$. Since these are basic concepts which also appear in other fields of perturbative QCD, the relations may be useful.

5 Concluding Remarks

The first part of this lecture was devoted to an overview of perturbative QCD from a modern viewpoint. We explained the theoretical formulation, in which the following subjects were covered: (a) The relation between purely perturbative predictions and predictions based on OPE of EFTs. (b) Computational methods for higher-order corrections, which also give solid foundations to EFTs. (c) Roles of singularities in Feynman amplitudes therein. (See Sec. 3.6 for the summary of the first part.) We tried to give a unified view in terms of singularities in amplitudes.

Contrastingly, in the current status it is difficult to present an overview of diverse physics phenomena described by perturbative QCD from a unified viewpoint. By the same token, when applying the above theoretical formulation to each of these phenomena, one needs to adapt the formulation by incorporating specific features of the system of interest, even though the basic concept is general. For example, the relevant dynamical degrees of freedom depend on the system and it happens that almost as many varieties

of evolution equations appear as the number of different subjects of perturbative QCD. The differences consist in which dynamical variables are relevant and which variables have been integrated out; (in an ultimate form of the theory) it is hoped that each of them can be cast into an EFT in general as described in this lecture. Analyses based on singularities in amplitudes are useful in developing an EFT, after the procedure of its construction is clarified or in the process of clarifying it.

In the latter part of this lecture we reviewed an application of perturbative QCD to heavy quarkonium systems, in particular to bottomonium states and the static QCD potential. It is interesting that different theoretical frameworks and various concepts are mutually linked and converge towards a consistent picture. Namely, IR renormalons in the purely perturbative computation, OPE in an EFT, and separation of IR contributions after log resummations, all point to a consistent result, which also agrees with lattice results. At the same time we find an interrelation between the concepts of the running coupling constant, linear potential and quark self-energies (which resemble constituent quark masses) from a microscopic viewpoint, although the validity range is restricted to the short-distance region $r \lesssim \Lambda_{\text{QCD}}^{-1}$. (See Sec. 4.4 for lessons drawn from the latter part.) In principle, we expect that similar consistency checks can be carried out in applications of perturbative QCD to other physical systems.

As stated, we focused on singularities in Feynman amplitudes to present a unified view. As one carries out higher-loop computations explicitly, one realizes that the computations are composed by series of processes of resolution of singularities. Using known algorithms* one resolves entangled singularities in loop integrals step by step. As a result, for instance, the structure of the singularities is encoded in the characters (λ_i s) of generalized MZVs in the final results of radiative corrections. It is a goal of current researches to reveal the encoding mechanism and as a consequence find an efficient way of computation. In dimensional regularization separation of multiple scales in a physical process is also determined by the structure of singularities (analyticity) of each amplitude. We can perform scale separation not only by using poles of propagators but also by using the singularity of order Λ_{QCD} generated by log resummations. We pointed out the usefulness of this method in renormalizing Wilson coefficients at IR.

Although barely covered in this lecture, presently rapid progress is made in the field related to LHC physics, such as automatization of computations of radiative corrections and developments of computational tools by combining them with MC simulation programs. It is expected that multitudes of computations for high energy processes including radiative corrections will be achieved in near future. We look forward to see how these developments will lead to new physics insights.

A partial list of other future developments expected in perturbative QCD is as follows.

- (a) Predictions in collaboration with lattice computations. They would be indispensable for perturbative QCD to become a high precision science.

* For instance, the author uses combinations of the Laporta algorithm, method of differential equation, method of Mellin-Barnes integral representation, reduction of multiple sums and integrals, and shuffle relations, etc., in analytic evaluations of higher-loop computations.

- (b) Understanding the essence of radiative corrections, such as finding solutions to the questions raised in Sec. 3.5.
- (c) Systematic construction of EFTs (without recourse to diagrammatic methods). Since the present methods for constructing EFTs require considerable expertise, for general education it is desirable to develop a transparent method in a field theoretical approach.
- (d) To establish a general prescription for resummation of logarithms and separation of IR contributions for an arbitrary OPE.

Although perturbative QCD has made significant progress over the years, there exist certain observables whose perturbative expansions do not exhibit expected convergence behaviors, for reasons not well understood. It is necessary to investigate them in detail, where brute-force computations of higher-order corrections would not suffice. For example, it may be similar to the case of the static potential before canceling the leading renormalon in the r -independent constant. (See Fig. 17.) There are many studies to be done, and we would like to see more flows towards unification of perturbative QCD.

Acknowledgements

The author would like to dedicate this lecture to the late Prof. Jiro Kodaira, who was leading the community of perturbative QCD in Japan. The author is grateful to the organizers of “QCD Club,” in particular to K. Fukushima, for giving the opportunity of this lecture. This work was supported in part by Grant-in-Aid for scientific research No. 23540281 from MEXT, Japan.

Appendix: Proof of Eq. (44)

We give a proof of Eq. (44):

$$V_{\text{UV}}(r; \mu_f) - [V_C(r) + \sigma r] = \text{const.} + \mathcal{O}(\mu_f^3 r^2). \quad (48)$$

$V_{\text{UV}}(r)$ is defined in Eq. (43). After integrating over the angular variables, it can be expressed as a one-parameter integral in the range $\mu_f < q < \infty$:

$$V_{\text{UV}}(r; \mu_f) = -\frac{2C_F}{\pi} \int_{\mu_f}^{\infty} dq \frac{\sin qr}{qr} \alpha_V(q) = -\frac{2C_F}{\pi} \text{Im} \int_{\mu_f}^{\infty} dq \frac{e^{iqr}}{qr} \alpha_V(q). \quad (49)$$

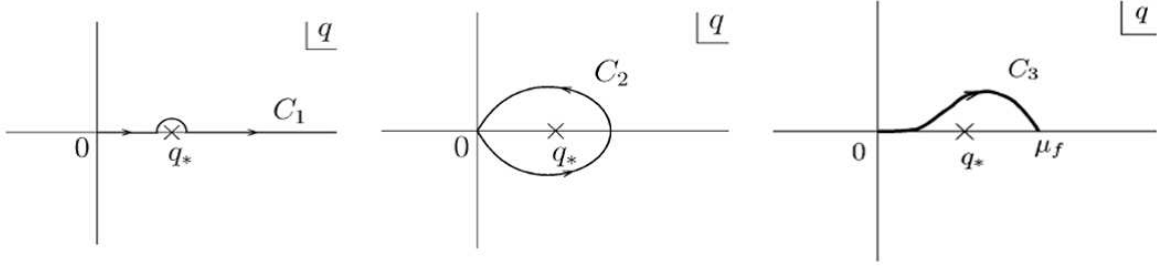


Figure 26: Contours C_1 , C_2 and C_3 of integrals in Eq. (50).

The formulas for $V_C(r)$ and σr are given as contour integrals in the complex q -plane by Eqs. (37) and (38). Hence, the difference can be written as

$$V_{UV}(r; \mu_f) - [V_C(r) + \sigma r] = \frac{C_F}{\pi i} \int_{C_2} dq \frac{\alpha_V(q)}{qr} + \frac{2C_F}{\pi} \text{Im} \int_{C_3} dq \frac{e^{iqr}}{qr} \alpha_V(q) - \sigma r. \quad (50)$$

See Fig. 26 for the contours C_1 , C_2 , C_3 . Since $\mu_f r \ll 1$, along the contour C_3 we can expand the Fourier factor as $e^{iqr} = 1 + iqr + \frac{1}{2}(iqr)^2 + \dots$. Then we can rewrite the first and third terms as

$$\frac{2C_F}{\pi} \text{Im} \int_{C_3} dq \frac{\alpha_V(q)}{qr} = -\frac{C_F}{\pi i} \int_{C_2} dq \frac{\alpha_V(q)}{qr}, \quad (51)$$

$$\frac{2C_F}{\pi} \text{Im} \int_{C_3} dq \left(-\frac{1}{2}qr\right) \alpha_V(q) = -\frac{C_F}{\pi i} \int_{C_2} dq \left(-\frac{1}{2}qr\right) \alpha_V(q). \quad (52)$$

These terms are canceled and the rest has a form $\text{const.} + \mathcal{O}(\mu_f^3 r^2)$, which completes the proof. It is in the above equations, when the contour C_3 is changed to C_2 , that μ_f dependences of the ‘‘Coulomb’’+linear terms are shown to vanish. The same change of contour does not apply to the constant and r^2 terms (due to existence of i), hence the μ_f dependence remain in these terms.

In essence, the above proof can be interpreted as follows. IR contributions in $V_{QCD}(r)$ can be subtracted as contour integrals along C_3 near the IR singularity $q = q_*$ of $\alpha_V(q)$. It is possible to decompose $V_{UV}(r; \mu_f)$ into the form close to Eq. (28). The parts which are sensitive to the IR cut-off μ_f are the parts which can be absorbed into the pole mass or the non-perturbative matrix elements. $V_C(r)$ and σr have forms genuinely UV; it is consistent since there are no IR operators which can absorb the IR part of these r dependences.

References

- [1] J. Kodaira, ‘‘QCD: Past, Present and Future,’’ based on the talk in Symposium ‘‘30 years of QCD’’ at Japan Physics Society Meeting, at Tokyo University of Science, Noda, Mar. 2005, <http://www.jahep.org/hepnews/2005/Vol124No2-2005.7.8.9kodaira.pdf> (in Japanese).

- [2] “Perturbative Quantum Chromodynamics,” ed. A. H. Mueller, (World Scientific, Singapore, 1989).
- [3] R. K. Ellis, W. J. Stirling and B. R. Webber, “QCD and collider physics,” Camb. Monogr. Part. Phys. Nucl. Phys. Cosmol. **8** (1996) 1.
- [4] J. Collins, “Foundations of perturbative QCD,” (Cambridge monographs on particle physics, nuclear physics and cosmology. 32).
- [5] A. V. Manohar and M. B. Wise, “Heavy quark physics,” Camb. Monogr. Part. Phys. Nucl. Phys. Cosmol. **10** (2000) 1.
- [6] N. Brambilla, A. Pineda, J. Soto and A. Vairo, “Effective field theories for heavy quarkonium,” Rev. Mod. Phys. **77** (2005) 1423 [hep-ph/0410047].
- [7] V. A. Smirnov, “Evaluating Feynman integrals,” Springer Tracts Mod. Phys. **211** (2004) 1.
- [8] J. C. Collins, D. E. Soper and G. F. Sterman, Adv. Ser. Direct. High Energy Phys. **5** (1988) 1 [hep-ph/0409313]. (The first chapter of [2].)
- [9] N. Brambilla *et al.* [Quarkonium Working Group Collaboration], hep-ph/0412158.
- [10] N. Brambilla, S. Eidelman, B. K. Heltsley, R. Vogt, G. T. Bodwin, E. Eichten, A. D. Frawley and A. B. Meyer *et al.*, Eur. Phys. J. C **71** (2011) 1534 [arXiv:1010.5827 [hep-ph]].
- [11] C. Bogner and S. Weinzierl, Comput. Phys. Commun. **178** (2008) 596 [arXiv:0709.4092 [hep-ph]].
- [12] T. Binoth and G. Heinrich, Nucl. Phys. B **585** (2000) 741 [hep-ph/0004013].
- [13] T. Binoth and G. Heinrich, Nucl. Phys. B **680** (2004) 375 [hep-ph/0305234].
- [14] V. A. Smirnov, “Applied asymptotic expansions in momenta and masses,” Springer Tracts Mod. Phys. **177** (2002) 1.
- [15] M. Beneke, Phys. Rept. **317** (1999) 1 [hep-ph/9807443].
- [16] M. Beneke and V. M. Braun, Phys. Lett. B **348** (1995) 513 [hep-ph/9411229].
- [17] K. G. Chetyrkin and F. V. Tkachov, Nucl. Phys. B **192**, 159 (1981).
- [18] B. Jantzen, JHEP **1112** (2011) 076 [arXiv:1111.2589 [hep-ph]].
- [19] S. Laporta and E. Remiddi, Phys. Lett. B **379** (1996) 283 [hep-ph/9602417].
- [20] T. Aoyama, M. Hayakawa, T. Kinoshita and M. Nio, Phys. Rev. Lett. **109** (2012) 111807 [arXiv:1205.5368 [hep-ph]].

- [21] A. B. Goncharov, *Multiple polylogarithms and mixed Tate motives*, arxiv:math.AG/0103059.
- [22] T. Terasoma, *Mixed Tate motives and multiple zeta values*, Invent. Math. **149** (2002) 339.
- [23] P. Deligne and A. Goncharov, *Groupes fondamentaux motiviques de Tate mixte*, Ann. Sci. Ecole Norm. Sup. (4) **38** (2005) 1.
- [24] K. Ihara, M. Kaneko, and D. Zagier, *Derivation and double shuffle relations for multiple zeta values*, Compos. Math., **142** (2006) 307.
- [25] C. Anzai and Y. Sumino, J. Math. Phys. **54** (2013) 033514 [arXiv:1211.5204 [hep-th]].
- [26] D. J. Broadhurst, hep-th/9604128.
- [27] D. J. Broadhurst, Eur. Phys. J. C **8** (1999) 311 [hep-th/9803091].
- [28] F. Brown and O. Schnetz, arXiv:1006.4064 [math.AG].
- [29] E. Remiddi, Nuovo Cim. A **110** (1997) 1435 [hep-th/9711188].
- [30] ATLAS Group, <https://twiki.cern.ch/twiki/bin/view/AtlasPublic/StandardModelPublicCollisionPlots>.
- [31] J. Beringer *et al.* [Particle Data Group Collaboration], Phys. Rev. D **86** (2012) 010001.
- [32] [ATLAS and CDF and CMS and D0 Collaborations], arXiv:1403.4427 [hep-ex].
- [33] C. Anzai, Y. Kiyo and Y. Sumino, Phys. Rev. Lett. **104**, 112003 (2010).
- [34] A. V. Smirnov, V. A. Smirnov and M. Steinhauser, Phys. Rev. Lett. **104**, 112002 (2010).
- [35] S. Necco and R. Sommer, Nucl. Phys. B **622**, 328 (2002).
- [36] T. T. Takahashi, H. Suganuma, Y. Nemoto and H. Matsufuru, Phys. Rev. D **65**, 114509 (2002).
- [37] S. Aoki *et al.* [JLQCD Collaboration], Phys. Rev. D **68**, 054502 (2003).
- [38] U. Aglietti and Z. Ligeti, Phys. Lett. B **364**, 75 (1995).
- [39] A. Pineda, Ph.D. Thesis, <http://www.slac.stanford.edu/spires/find/hep/www?irn=5399084>.
- [40] A. H. Hoang, M. C. Smith, T. Stelzer and S. Willenbrock, Phys. Rev. D **59**, 114014 (1999).

- [41] M. Beneke, Phys. Lett. B **434**, 115 (1998).
- [42] K. G. Chetyrkin, B. A. Kniehl and M. Steinhauser, Phys. Rev. Lett. **79** (1997) 2184 [hep-ph/9706430].
- [43] Y. Sumino, Phys. Rev. D **65**, 054003 (2002).
- [44] N. Brambilla, A. Pineda, J. Soto and A. Vairo, Phys. Rev. D **60**, 091502 (1999).
- [45] Y. Sumino, Phys. Lett. B **595** (2004) 387 [hep-ph/0403242].
- [46] Y. Sumino, Phys. Lett. B **571** (2003) 173 [hep-ph/0303120].
- [47] Y. Sumino, Phys. Rev. D **76**, 114009 (2007).
- [48] A. Pineda, J. Phys. G **29**, 371 (2003);
- [49] Y. Kiyo and Y. Sumino, Phys. Lett. B **730** (2014) 76 [arXiv:1309.6571 [hep-ph]].
- [50] N. Brambilla, Y. Sumino and A. Vairo, Phys. Lett. B **513** (2001) 381.